主論文

NONLINEAR MHD WAVE PROPAGATION IN THE SOLAR CHROMOSPHERE, I

The Case of Uniform Vertical Magnetic Field

Kazunari SHIBATA

Department of Earth Science, Aichi University of Education,

Kariya, Aichi 448, Japan

To be Published in

Publ. Astron. Soc. Japan (1983), Vol. 35, No. 2

Abstract

Two dimensional MHD simulations are performed in order to elucidate the nonlinear propagation of MHD waves in the solar chromosphere. A sudden pressure enhancement is assumed to occur in a small region in the upper photosphere which is subject to a uniform vertical magnetic field. The field strength (B_0) is taken to be a free parameter. It is shown that in the case of $\beta_A > 1$ ($\beta_A = 8\pi p/B_0^2$ is the ratio of gas pressure to magnetic pressure at the level of initial pressure enhancement) a sound-like fast mode generated by the initial pressure enhancement splits into a magnetic fast mode and an acoustic slow mode when it propagates upward into a low β (< 1) region. The energy is mainly transformed into the acoustic slow mode. Near the region of the initial pressure enhancement a vortex motion appears due to buoyancy. On the other hand, in the case of $\beta_A < 1$, an acoustic slow mode and a magnetic fast mode are directly produced by the initial pressure enhancement and there occurs no vortex motion. The upward propagations of the acoustic slow mode are almost along the magnetic field and well approximated by one-dimensional hydrodynamics. Applications of these results to the origin of the inhomogeneous and dynamical structure of the solar chromosphere and the problem of chromospheric and coronal heating are briefly discussed.

Key words: Atmospheric heating, Chromospheric structure, MHD waves, Mode coupling

1. Introduction

The solar atmosphere is filled with many wave phenomena. Some of them, such as five minute oscillations, are rooted in the convection zone (e.g. Ando and Osaki, 1975; Deubner, 1977), and some of them are generated by explosive phenomena; for example, Moreton waves are believed to occur from flares (Uchida, 1968). It is very important to make clear the physics of these wave phenomena not only because they are important constituents in many solar phenomena but also because they may play fundamental roles in the origin of the inhomogeneous atmospheric structure and in the energy balance of the atmosphere.

As for nonlinear MHD wave propagation in the corona, many two-dimensional MHD simulations have been performed (Nakagawa et al., 1978; Wu et al., 1978; Steinolfson et al., 1978; Dryer et al., 1979; Nakagawa et al., 1981). However, as for MHD waves in the chromosphere no one has tried to perform nonlinear two-dimensional simulations. It is the primary purpose of this paper to present the first numerical two-dimensional simulations of MHD waves in the chromosphere.

There are some essential differences between the physics of MHD wave propagations in the corona and that in the chromosphere. For example, in many cases the plasma β^* (the ratio of gas pressure to magnetic pressure = $8\pi p/B^2$) increases with height in the corona, whereas in the chromosphere β^* decreases with height. This is due to the large difference of the pressure scale height in both layers. At the photospheric level, we have $\beta^* \gg 1$ in the non-magnetic region and $\beta^* \lesssim 1$ in the magnetic region. On the other hand, at the low coronal level, we have $\beta^* \ll 1$ more or less everywhere. Thus, the level of $\beta^* = 1$ exists between the photosphere (or sub-photosphere) and the low corona. This paper mainly studies the influence of height variation of β^* on MHD wave propagation in the chromosphere, especially elucidates the mode exchange of MHD waves

at the level of $\beta^* \approx 1$.

Recently, Suematsu et al. (1982) showed by performing one-dimensional hydrodynamic simulations that spicules could be produced by acoustic shock waves (MHD slow mode shocks) which originate from a bright point appearance (a sudden increase in pressure) at the network in the photosphere or in the low chromosphere. It is also suggested that the same mechanism as in the case of spicules might work for small surges associated with Ellerman bombs (Shibata et al., 1982), for EUV macrospicules unseen in $H\alpha^*$ (Shibata, 1982) and for fibrils and threads (Suematsu, 1982). Since at the photospheric level β^* is near unity even in strong magnetic flux tubes as mentioned above, the one-dimensional treatment made in these previous numerical simulations may not be nescessarily correct. This paper also studies the validity and the limitation of these one-dimensional hydrodynamic simulations, by comparing them with our present two-dimensional ones. This paper describes only the case of uniform vertical magnetic field. The case of more realistic field configurations will be studied in a subsequent paper.

Section 2 gives assumption, basic equations and numerical procedures. The typical cases of weak (B_0 = 90.7 G) and strong (B_0 = 907 G) field strengths are investigated in detail in sections 3 and 4, respectively. Summary of other cases and comparison of our simulations with one-dimensional hydrodynamic simulations made before are given in section 5. In section 6, energy transfer by slow and fast mode MHD waves is studied by a rough approximate method. Finally, in section 7 conclusions are summarized and applications of our results to the origin of spicule-like chromospheric fine structures and to the problem of the chromospheric and coronal heating are briefly discussed.

2. Basic Equations and Method

We assume the simplest situation in studying MHD waves in the solar atmosphere, i.e. (1) the gas motion is two dimensional with infinite homogeneity in one direction in the horizontal plane, (2) the electrical conductivity is infinite, and (3) the motion occurs adiabatically. In Cartesian coordinates, basic equations are

$$\frac{\partial \rho^{\ddagger}}{\partial t} + \frac{\partial}{\partial x}(\rho^{\ddagger} v_x) + \frac{\partial}{\partial y}(\rho^{\ddagger} v_y) = 0, \qquad (1)$$

$$\frac{\partial}{\partial t}(\rho^{\ddagger} v_x) + \frac{\partial}{\partial x}\left[\rho^{\ddagger} v_x^2 + p + \frac{1}{8\pi^{\ddagger}}(B_y^2 - B_x^2)\right] + \frac{\partial}{\partial y}\left[\rho^{\ddagger} v_x v_y - \frac{B_x B_y}{4\pi^{\ddagger}}\right] = 0, \qquad (2)$$

$$\frac{\partial}{\partial t}(\rho^{\ddagger} v_y) + \frac{\partial}{\partial x}\left[\rho^{\ddagger} v_x v_y - \frac{B_x B_y}{4\pi^{\ddagger}}\right] + \frac{\partial}{\partial y}\left[\rho^{\ddagger} v_y^2 + p + \frac{1}{8\pi^{\ddagger}}(B_x^2 - B_y^2)\right] + \rho^{\ddagger} g = 0, \qquad (3)$$

$$\frac{\partial B_x}{\partial t} + \frac{\partial}{\partial y}(v_y B_x - v_x B_y) = 0, \qquad (4)$$

$$\frac{\partial B_y}{\partial t} + \frac{\partial}{\partial x}(v_x B_y - v_y B_x) = 0, \qquad (5)$$

$$\frac{\partial}{\partial t}\left[\frac{p}{\gamma^{\ddagger}-1} + \frac{1}{2}\rho^{\ddagger}(v_x^2 + v_y^2) + \frac{1}{8\pi^{\ddagger}}(B_x^2 + B_y^2)\right] + \frac{\partial}{\partial x}\left[\frac{\gamma^{\ddagger}}{\gamma^{\ddagger}-1} p v_x + \frac{1}{2}\rho^{\ddagger} v_x(v_x^2 + v_y^2) + \frac{B_y}{4\pi^{\ddagger}}(v_x B_y - v_y B_x)\right] + \frac{\partial}{\partial y}\left[\frac{\gamma^{\ddagger}}{\gamma^{\ddagger}-1} p v_y + \frac{1}{2}\rho^{\ddagger} v_y(v_x^2 + v_y^2) + \frac{B_x}{4\pi^{\ddagger}}(v_y B_x - v_x B_y)\right] + \rho^{\ddagger} g v_y = 0. \qquad (6)$$

Here, t is the time, x the horizontal coordinate, y the vertical coordinate, ρ the density, p the gas pressure, v_x and v_y components of the velocity, B_x and B_y components of magnetic field strength, γ (= 5/3) the specific heat ratio, g the gravitational acceleration in the solar atmosphere, which is assumed to be constant, 2.74 x 10^4 cm s^{-2}. These equations are solved numerically by the modified Lax-Wendroff scheme (Rubin and Burstein, 1967).

The regions considered in this paper are the chromosphere and the photosphere. The initial unperturbed density and pressure distributions are calculated from the temperature distribution in the HSRA model (Gingerich et al., 1971) so that the atmosphere is in hydrostatic equilibrium. As for the initial magnetic field configuration, we assume a uniform vertical field and take five cases of different field strengths, i.e. B_0 = 907, 383, 181, 90.7 and 0 Gauss. The origin of the vertical coordinate is taken at the base level of the photosphere (i.e. the level of τ_{5000} = 1).

A pressure enhancement is introduced at t = 0 within a circular region around (x_0, y_0) with radius R_0 in the following way,

$$p(x,y) = p_0(x,y)\ [\ 1 + (p_m/p_0 - 1)\ [\ 1 + \cos(\pi R/R_0)\ ]/2\ ], \quad (7)$$

where $R = [(x-x_0)^2 + (y-y_0)^2]^{1/2}$, $p_0(x,y)$ is the hydrostatic pressure distribution, (x_0,y_0) is the central point of the pressure enhancement region, p_m/p_0 is the maximum value of the pressure increase ratio. This initial pressure enhancement produces an approximate sinusoidal (pulse) wave with wavelength of $2R_0$ if the medium is homogeneous. In this paper, R_0 = 150 km, p_m/p_0 = 1.5 and y_0 = 345 km are fixed. Our computational domain ranges from (L_x x L_y) = (1200 km x 750 km) for strong field cases to (1800 km x 1200 km) for weak field cases. The grid sizes Δ x and Δ y are equally set to 15 km, which is about tenth of the scale height. The time step Δ t is computed step by step so that the CFL condition is satisfied. Since our problem is symmetrical on the vertical line passing

through the central point (x_0, y_0) of the initial pressure enhancement, the simulations are performed only in the left half of the whole domain.

Figure 1

Figure 1 shows the vertical distribution of β' (solid curves) and the Alfven velocity v_A (dashed curves with dot) for two cases of B_0 = 90.7 G and 907 G. From this figure we see that in the case of B_0 = 90.7 G the height where the magnetic pressure becomes equal to the gas pressure ($y_{\beta'=1}$) is about 670 km and higher than the level of the initial pressure enhancement (y_0 = 345 km), whereas in the case of B_0 = 907 G, $y_{\beta'=1}$ is about 180 km and lower than y_0. In other words, β'_* (β' at y_0) > 1 for B_0 = 90.7 G while $\beta'_* < 1$ for B_0 = 907 G. This difference in $y_{\beta'=1}$ (or β'_*) between two cases causes an important difference in the propagation of MHD waves for each case, which is described in detail in later sections.

All boundaries are assumed to be 'free' boundaries where the fluid and waves can freely pass through beyond there. Technically, the design of an ideal free boundary is very difficult especially for two (and three) dimensional problems (e.g. Roache, 1972; Chu, 1978; Sato and Hayashi, 1979; Shibata, 1981). Although some efforts have been made in order to construct a physically self-consistent boundary condition for multi-dimensional mixed initial and boundary value problems (e.g. Nakagawa, 1980, 1981a,b), it has not yet been established what is the best condition for an ideal free boundary in the multi-dimensional problems. Therefore, and since the phenomena until MHD waves reach the boundaries are our main interest, we adopt the following simple boundary condition, i.e.

$$\frac{\partial \delta w}{\partial y} = 0 \qquad \text{for upper and lower boundaries,}$$

$$\frac{\partial \delta w}{\partial x} = 0 \qquad \text{for lateral boundaries,}$$

where $\delta w = w(t + \Delta t) - w(t)$ and w represents the variable ρ, v_x, v_y, B_x, B_y, and p. The reason why we have not adopted simpler conditions

$$\frac{\partial w}{\partial x} = 0, \frac{\partial w}{\partial y} = 0,$$

is that the unperturbed medium is strongly stratified. The adopted boundary condition is sufficient for the lower and lateral boundaries, but unsatisfactory for the upper boundary. In the following sections, we will show only the results that are not strongly influenced by the upper boundary condition.

Finally the cases are briefly considered where a pressure enhancement is introduced isotropically in a small region in the three dimensional space. In these cases, the behavior of the gas can be examined two-dimensionally in terms of the cylindrical coordinate whose z-axis is in the vertical direction. The place of the pressure enhancement is taken on the vertical axis as $r_0 = 0$ with a certain z_0. The basic equations to be used in these cases are obtained from equations (1)-(6) by the following way. That is, (x,y) should be read as (r,z). In addition, the following terms should be added to the left hand sides of equations (1)-(6) in order:

$$S_1 = \frac{\rho v_r}{r},$$

$$S_2 = \frac{1}{r}\left(\rho v_r^2 - \frac{B_r^2}{4\pi}\right),$$

$$S_3 = \frac{1}{r}\left(\rho v_r v_z - \frac{B_r B_z}{4\pi}\right),$$

$$S_4 = 0,$$

$$S_5 = -\frac{1}{r}\left(v_z B_r - v_r B_z\right),$$

and

$$S_6 = \frac{1}{r}\left[\frac{\gamma}{\gamma-1} p v_r + \frac{\rho v_r}{2}\left(v_r^2 + v_z^2\right) + \frac{B_z}{4\pi}\left(v_r B_z - v_z B_r\right)\right].$$

Some numerical results obtained in the above axially symmetric cases will be mentioned in section 5 in order to see how the difference of geometry influences the results.

The accuracy of our numerical simulations has been checked by various methods. For example, the maximum value of the numerical error for div $\mathbf{B} = 0$ is an order of $10^{-4} \sim 10^{-3}\ B_0/\Delta x$ in the worst case. This value is small enough for our main purpose.

3. The Case of Weak Field (B_0 = 90.7 G)

In this section, we show a typical example in the case of a weak magnetic field, i.e. B_0 = 90.7 G. This case is characterized by β^* = 19.8 and $y_{\beta=1}$ = 670 km ($> y_0$ = 345 km).

3.1. MHD Wave Propagation

Figures 2 and 3 show the time evolution of the disturbance produced by the initial pressure enhancement specified by equation (7). Figures 2 represent the contour of equal gas pressure increment ratio, $\Delta p/p_0$ ($\Delta p = p - p_0$), at t = 0, 16.49, 32.98 and 49.46 sec, where solid and dashed curves indicate positive and negative Δp respectively. The interval of level of adjacent contour curves is 0.02 in units of p_0. Figures 3 denote the velocity field at t = 16.49, 32.98 and 49.46 sec, and the magnitude of the velocity is indicated in the upper left part of figure 3 (a). Only velocities greater than 0.1 km s^{-1} are shown.

Figure 2

Figure 3

The disturbance is almost the same as sound waves (i.e. the fast mode MHD wave where $\beta^* > 1$) and the front propagates isotropically when time $<$ 32.98 sec (figure 2 a-c), although the magnitudes of the pressure increment ratio and the velocity show strong anisotropy due to the stratification effect. Note that as the waves enters the region of $\beta^* < 1$ ($y > 670$ km) the shape of the wave front deviates from a circle (figure 2d) and a small velocity field (≈ 0.2 km s^{-1}) perpendicular to the vertical magnetic field appears (figure 3c). This represents the generation of the magnetic fast mode in low β^*

media. At this stage the motion in the pressure maximum region is considered as the acoustic slow mode ($\Delta p/p_0 \approx 1.0$ and $v_{max} \approx 2.1$ km s^{-1}). We see small pressure depression ($\Delta p/p_0 \approx -0.03$) just ahead of the pressure maximum. This is because the high pressure region where the slow mode exists broadens the field line intervals and this perturbation of field lines propagates faster than the slow mode as the fast mode. That is, the fast mode just ahead of the slow mode is not a compression wave but a rarefaction wave.

Figure 4

Figures 4 show two dimensional spatial distributions of magnetic field strength ($B = (B_x^2 + B_y^2)^{1/2}$), velocity, field lines and gas pressure at t = 57.68 sec, where all quantities except for velocity and field lines are represented by the increment ratio, i.e. $\Delta w/w_0$ ($\Delta w = w - w_0$). The front of the magnetic fast mode has already propagated upward beyond the upper boundary (figure 4b), while the acoustic slow wave is now propagating in the illustrated region due to the slow propagating speed. It should be noted that the velocity vectors near the upper boundary ($1100 \lesssim y \lesssim 1200$ km) in figure 4b are not reliable due to the insufficient upper boundary condition. The same is true for the gas pressure near the upper boundary in figure 4d. At the epoch of t = 57.68 sec the magnitudes of gas pressure ($p \approx 2.2\ p_0$) and velocity (≈ 2.5 km s^{-1}) at the point of the acoustic slow mode maximum are larger than those at earlier epoch. The total pressure ($p + B^2/8\pi$) at the slow mode maximum, however, almost unchanges with time, i.e. the large gas pressure is compensated by the small magnetic pressure due to lateral broadening of field line intervals.

The vortex motion (figure 4b) causes the largest broadening of field line intervals (figure 4c). The local maximum of $\Delta p/p_0$ (figure 4d) just below the slow mode maximum is a kind of contact surface. This is produced by an upward movement of fluid element which has originally large pressure.

In order to see more intuitively how the acoustic slow wave in low β region is generated from the acoustic fast mode in high β region, we show in figures 5 some three dimensional plots of $\Delta p/p_0$ in order of time development. Figure 5a is the case of $B_0 = 0$ G, which is added for comparison, and figure 5b is the present case ($B_0 = 90.7$ G). It is evident that two cases are almost the same when $t < 16$ sec, but very different after 49 sec. Magnetic fields in a region of $\beta < 1$ confine a sound wave (i.e. the slow mode) into a very narrow region and enables it to propagate almost one-dimensionally in the vertical direction. It should be noted again that the results near the upper boundary (especially ≈ 6 grid points near the upper boundary of the figure at 80.60 sec in figure 5b) are not reliable due to the insufficient upper boundary condition (section 2).

The propagation and growth of the slow mode in various cases are shown in section 5.

Figure 5

3.2. Vortex Motion Around the Initial Pressure Enhancement Region and Generation of Gravity Waves

We show in figures 6 later evolution of the vortex motion around the initial pressure enhancement region. All figures show the lower half of the calculated domain. The left column is the velocity field and the right one is the temperature increment ratio. The times are 73.41 sec, 94.28 sec, 113.53 sec, and 137.10 sec.

Figure 6

At t = 73.41 sec, we can see a counterclockwise vortex motion, which is seen already at t = 32.98 ~ 57.68 sec. As time proceeds, the velocity of the vortex motion becomes small (t = 94.28 sec) and finally the direction of the vortex motion reverses (t = 113.53 sec). At t = 137.10 sec, we can see a well developed clockwise vortex motion, The shape of temperature enhancement region (i.e. bubble), which has initially a circular form, changes into a 'umbrella shape' at t = 73.41 sec, and the bubble is almost divided into two bubbles at t = 94.28 ~ 113.53 sec. But, due to the reversed vortex motion two bubbles merge again into one bubble at t = 137.10 sec.

We should stress that the vortex motion is strongly affected by the Lorentz force because an inequality $\rho v^2/2 < B^2/8\pi$ is satisfied. In order to understand this more clearly, we show in figures 7 the case of B_0 = 0 G for comparison. In figures 7, the reversing of vortex motion occurs at a distant place (t = 139.56 sec) from the original pressure enhancement region, and two bubbles never merge.

Figure 7

Although the evolution of the vortex motion and the bubble is somewhat different in two cases, the period of reversing motion in both cases is an order of about 200 sec, i.e. $\approx 2\pi/N_{BV}$, where N_{BV} is the Brunt-Väisälä frequency. This would be due to the smallness of the initial pressure enhancement ($p/p_0 = 1.5$). We can also see in figures 6 and 7 that small temperature enhancement propagates horizontally from bubble. This is considered to be a modified internal gravity wave. The horizontal propagating velocity (group velocity) of gravity wave is about 4 km s^{-1} for the case of B_0 = 90.7 G (figure 6) and 5.3 km s^{-1} for the case of B_0 = 0 G (figure 7), which are smaller than the sound velocity ($\approx$ 7 km s^{-1}) as shown in the linear theory (Stein and Leibacher, 1974).

The temperature oscillations in figures 6 are mainly due to the wave reflected at the lower and lateral boundaries. (Note that the constant phase surface of these oscillations is almost parallel to the boundaries.) That is, they are purely numerical. However, the amplitudes of the reflection waves are too small to significantly alter the physics of the inner region we are concerned with.

4. The Case of Strong Field (B_0 = 907 G)

In this section, we show a typical example in the case of strong field, i.e. B_0 = 907 G. This case is characterized by β^* = 0.198 (< 1) and $y_{\beta=1}$ = 180 km (< y_0 = 345 km) (see figure 1).

Figures 8 show the time evolutions (5.12 $\lesssim$ t $\lesssim$ 20.36 sec) of velocity field and of pressure increment ratio. It is remarkable that the region of the pressure enhancement almost unchanges its shape and only move upward slightly. This is because the strong magnetic field inhibits the large lateral expansion of matter and the explosion propagates almost one-dimensionally. That is, the motion of the region of the maximum pressure increment ratio is an acoustic slow wave from t = 0.

Figure 8

Although magnetic field lines are almost unchanged by the initial pressure enhancement (and so field lines are not shown), the magnetic fast mode with very small velocity amplitudes ($\lesssim$ 0.2 km s^{-1}) and small pressure increment ratio ($\Delta p/p_0 \approx$ 0.02) is also seen in figures 8. Since the Alfven velocity becomes larger in the upper chromosphere (figure 1) and the fast mode wave front area rapidly broadens as it propagates upward, the amplitude of physical quantities at the fast mode front becomes smaller as the time elapses.

The small local maximum of the pressure increment propagating downward is the acoustic slow mode, but this becomes indistinguishable soon by the following reasons. The wave amplitude decreases due to the stratification effect. Furthermore, below $y_{\beta=1}$ = 180 km the magnetic

pressure is smaller than the gas pressure and thus both magnetic fast mode and acoustic slow mode merges into one sound wave.

A 'bubble' generated from the initial pressure enhancement is confined into a narrow region by the strong magnetic field and there is no vortex motion (figures 8). We could not find any noticeable order of generation of internal gravity waves.

5. Summary of Other Cases and Comparison with One-Dimensional Hydrodynamic Computations

Before summarizing results of other cases, we show in figure 9 the time variations of some physical quantities at the explosion point. Solid curves show the case of B_0 = 90.7 G and dashed curves show the case of B_0 = 907 G. In these figures, v_y is the vertical velocity component, B_y the vertical component of field strength, p the gas pressure, ρ the density, T the temperature, and the subscript 0 denotes the initial value of these quantities. We see that in both cases all the quantities rapidly change during $0 \leq t \leq 15$ sec. This stage is considered as the 'explosive phase'.

In the case of B_0 = 90.7 G (solid curves), v_y increases again after about 20 sec and reaches a maximum ($\approx$ 0.95 km s^{-1}) at $t \approx$ 48 sec, and thereafter it decreases. On the other hand, in the case of B_0 = 907 G (dashed curves), v_y has no secondary maximum, and decreases monotonically. The time when v_y change its sign is about 111 sec for the case of B_0 = 90.7 G and about 78 sec for the case of B_0 = 907 G. From the detailed descriptions in the preceding sections, it is evident that the secondary maximum of v_y in the case of B_0 = 90.7 G is caused by the vortex motion due to buoyancy and the absense of the secondary maximum of v_y in the case of B_0 = 90.7 G is due to the inhibition of vortex motion by strong magnetic field. Note that during the 'buoyancy phase' in the case of B_0 = 90.7 G the field strength and the gas pressure are almost constant whereas the density and the temperature change oppositely each other. There is no significant oscillatory behavior on the time variation of those quantities for the case of B_0 = 907 G, although in one-dimensional hydrodynamic simulations we had a standing acoustic oscillations whose period is about 200 sec (acoustic cut-off period) if we perform simulation for long durations.

Figure 9

Table I

Table I shows the summary of our simulation results, which includes results of one-dimensional hydrodynamic (1HD) computation as the limiting case of $B_0 = \infty$. The method of 1HD computation is almost the same as that described in section 2. Table I includes also results obtained in the case of axially-symmetric pressure enhancements described at the end of section 2. These results are designated by rz (xy denotes the results in two-dimensional configurations in the Cartesian coordinates).

Since the delay of the time t_c when the vertical velocity at the explosion point changes its sign well reflects the strength of buoyancy as shown in figure 9, we show t_c of each case in Table I. As the field strength becomes smaller, t_c becomes longer, because the Lorentz force acting against the vortex motion becomes weaker. We see also that t_c in the rz case is smaller than that of the xy case. The reason is as follows. The buoyant gas in the rz case more easily escapes from the original explosion point due to the geometrical effect than in the xy case. Thus, the time when the quasi-static equilibrium is established is smaller in the rz case than in the xy case.

Figure 10

Figure 11

Let us now investigate the spatial growth of the vertical velocity at the wave front of the acoustic slow mode (or the acoustic fast mode if $\beta^{*} > 1$) during its propagation through the chromosphere. Figures 10 and 11 show the log-log plot of the non-dimensional velocity amplitude divided by the local unperturbed sound velocity (v_{amp}/c) against the unperturbed chromospheric density ρ^{*} (g cm^{-3}) at the height where the

wave passes. Figure 10 is for the xy case and figure 11 is for the rz case. It is evident that as the field strength becomes larger the curve approaches 1HD case. Furthermore in low β^* region the spatial growth rate of the amplitude of acoustic slow waves is approximately equal to that of 1HD case, i.e. $v_{amp}/c \propto \rho^{-0.33}$. The smaller growth rate than the case of one-dimensional linear waves ($v_{amp}/c \propto \rho^{-0.5}$) is due to shock dissipation ; these acoustic slow waves are already weak shocks. We see also that the growth rate of two-dimensional acoustic waves (shocks) is $v_{amp}/c \propto \rho^{-0.22}$ between $-0.5 \leq \log(v_{amp}/c) \leq -0.3$ (in the case of B_0 = 0 G of xy case) and that of axially-symmetric waves is $v_{amp}/c \propto \rho^{-0.11}$ between $-1.02 \leq \log(v_{amp}/c) \leq -0.9$ (in the case of B_0 = 0 G of rz case).

The last column in Table I denotes the ratio of the vertical velocity at the wave front of the acoustic slow mode (or the acoustic fast mode) to that of the acoustic wave in 1HD case at the height of 600 km. In the case of 90.7 G, an acoustic slow mode is not yet generated at y = 600 km because the wave is below the height of $\beta^* = 1$ (665 km), and thus v_{slow}/v_{1HD} is equal to that for the case of B_0 = 0 G (see also figure 10 and 11). The ratio of 0.93 (xy case) and 0.91 (rz case) for B_0 = 907 G indicates that energy consumed to produce the magnetic fast mode is less than 10 % of the total energy deposition. Note that the ratios in rz case are all smaller than those in xy case. This is due to the geometrical effect.

Since two dimensional MHD simulations require large computational time, we have not yet calculated the later evolution of the acoustic slow waves in our two dimensional simulations. In the case of 1HD, however, we have pursued 1HD simulations up to the time when a spicule is formed. The 1HD simulations in this paper is different from previous 1HD simulations (Suematsu et al., 1982; Shibata et al., 1982; Shibata and Suematsu, 1982) in the way of pressure enhancement. That is, in the present ones the pressure enhancement is given as the initial condition, whereas in the previous ones it is given as the boundary conition. As a result of this difference, in the

present ones the pressure enhancement at the explosion point disappears in a short time (see figure 9), while in the previous ones we can maintain the pressure enhancement at our disposal ; in fact in Suematsu et al.'s paper the duration of the pressure enhancement was assumed as 5 min.

In spite of this important difference the results of the present 1HD simulations are almost the same as those obtained by Suematsu et al. (1982). That is, the (slow mode) shock becomes stronger and stronger as it propagates upward, and finally collides with the chromosphere-corona interface. Then, the interface is ejected by this collision and its motion is approximately ballistic. This interface is interpreted as the top of the spicules (Suematsu et al., 1982). These dynamics are repeated at about an acoustic cut-off period ($\approx$ 200 sec) by subsequent shocks which originate from so called 'wake'. (Note that this 'wake' is also seen in two-dimensional results, e.g. see figure 5). The reason why the spicule dynamics is insensitive to the way of the pressure enhancement is that slow shocks, which drive spicules, are almost independent of the later evolution of the pressure enhancment once shocks are ejected from it (Shibata et al., 1982).

The maximum height of the spicule in the present 1HD simulations is about 5300 km. From the result of $v_{slow}/v_{1HD} = 0.91 \sim 0.93$ in the case of $B_0 = 907$ G, we can expect that the maximum height of the spicule in two-dimensional MHD case of $B_0 = 907$ G is about $(0.91^2 \sim 0.93^2) \times 5300$ km $= 4400 \sim 4600$ km because the growth of slow shocks is determined by density stratification alone if the cross-section of the magnetic flux tube is constant (Shibata and Suematsu, 1982a).

6. Energy Transfer by Slow and Fast Mode MHD Waves

Let us now consider the problem of energy transfer in the vertical direction by slow and fast mode MHD waves. Since the velocity amplitude associated with a weak magnetic fast mode is much smaller than the Alfven velocity in low β region, we can approximate the vertical component of energy flux of acoustic slow waves and that of magnetic fast waves respectively by

$$F_{slow} \approx \Delta p\, v_y, \qquad (8)$$

and

$$F_{fast} \approx -B_x B_{y0} v_x / 4\pi, \qquad (9)$$

where $\Delta p = p - p_0$. If we use linearized relations of MHD equations (1)-(6), equations (8) and (9) become $|F_{slow}| = \rho v_y^2 c$ and $|F_{fast}| = \rho v_x^2 v_A$, respectively. Note that in the high β region equation (8) represents the vertical component of energy flux of acoustic waves (fast mode).

In order to compare total energy transfer by the slow mode with that by the fast mode we integrate equations (8) and (9) in the horizontal direction throughout the whole domain where the numerical simulations were made. Figures 12 (a)-(c) show time variations of the horizontally integrated energy flow at several fixed heights in the xy case. (The results in rz case are essentially the same as these results). Figure 12 (a) is the case of $B_0 = 0$ G and so $F = F_{acoustic} = \Delta p\, v_y$. In figures 12 (b) (90.7 G) and 12 (c) (907 G), thick curves correspond to $F_{slow} = \Delta p\, v_y$ and thin curves $F_{fast} = -B_x B_{y0} v_x / 4\pi$, but if $\beta > 1$ thick curves represent $F_{acoustic}$ as mentioned above.

Figure 12

Close inspection of figures 12 (a)-(c) reveals that :

1) In the case of acoustic → slow + fast in figure 12 (b) (B_0 = 90.7 G), $\tilde{F}_{slow}$ ($\tilde{F} \equiv \int F\,dx$) is approximately equal to $\tilde{F}_{acoustic}$ of B_0 = 0 at least around its first maximum and $(\tilde{F}_{slow})_{max}/(\tilde{F}_{fast})_{max} \gtrsim 2$ for h = 750 km and 900 km. Considering the short duration for the magnetic fast mode pulse to pass a given height, we can say that almost all the energy of initial acoustic waves is transformed into the slow mode waves.

2) The secondary maximum appears in almost all the cases of Δp v_y. This possibly corresponds to the wake of acoustic pulse (for acoustic slow waves in low β' region and acoustic waves in high β'' region) (Lamb, 1932; Kato, 1966; Stein and Schwartz, 1972; Suematsu et al., 1982; Hollweg, 1982; see also figure 5). The large differences of the wake for different field strengths may be not only due to the physical origin but also due to the numerical origin (i.e. an insufficient upper boundary condition; see section 2).

3) $\tilde{F}_{fast}$ decreases more rapidly with height than $\tilde{F}_{slow}$. This is the results of strong refraction of the fast mode ray path. (v_A increases rapidly with height. See figure 1).

4) $\tilde{F}_{fast}$ is much smaller than $\tilde{F}_{slow}$ in figure 12 (c).
($(\tilde{F}_{slow})_{max}/(\tilde{F}_{fast})_{max} \gtrsim 10$.)

5) $\tilde{F}_{slow}$ in figure 12 (c) is slightly larger than $\tilde{F}_{acoustic}$ in (a). This meas that more energy is transported to the upward direction directly from the initial pressure enhancement in the case of the

presence of strong ($\gtrsim$ 363 G) field strength than in the case of $B_{0} = 0$ G.

Summarizing these results, we can conclude that in the region with vertical magnetic field (e.g. plages, supergranulation boundaries, sunspots) the energy of acoustic waves is transformed into the energy of acoustic slow mode at the level of $\beta' \approx 1$ when the waves travel from high β' region to low β' region. If the acoustic generator is embedded in a strong field ($\beta' \lesssim 1$) medium, the efficiency of its upward propagation (or propagation along field lines) increases.

Let us consider the physical reason of the above results. It is easy to understand the former result in the above paragraph if we consider the following example. Suppose a plane acoustic wave propagating upward in the exactly vertical direction in a stratified atmosphere subject to a uniform vertical magnetic field. In this example, the background magnetic field does not exert any force on the wave motion of gas because the oscillating direction of gas in the acoustic wave is exactly parallel to the magnetic lines of force. Thus, the acoustic wave, which is originally an acoustic 'fast wave' in high β' media, remains an acoustic wave even if it enters the low β' media where we call the acoustic wave as the acoustic 'slow wave'.

An important result of our numerical experiment is that even if the original direction of the wave vector of a plane wave component of an acoustic wave is not exactly parallel to the magnetic lines of force the acoustic wave become mainly an acoustic slow wave. Therefore, there is a critical angle of the ray direction of the wave within which almost all the energy of an acoustic wave is transformed into that of an acoustic slow mode. We can approximately estimate this critical angle from figures 3 and 4 to be an order of 10 degree, though more exact treatment is necessary. Furthermore, it will be necessary

to compare our results with previous detailed studies on the mode exchange of MHD waves for both linear (e.g. Stein, 1971) and nonlinear case (e.g. Pikelner and Livshitz, 1964; Kaburaki and Uchida, 1971), which is our future work.

7. Summary and Discussion

In this paper, we have investigated nonlinear MHD wave propagations in the solar chromosphere with a uniform vertical magnetic field. Main results are summarized as follows :

(1) An acoustic wave propagating upward in high β' media splits into a magnetic fast mode and an acoustic slow mode at the level of $\beta'' = 1$. In this process, the energy flux of the original acoustic wave is mainly transformed into the energy flux of the acoustic slow mode.

(2) If an initial pressure enhancement occurs isotropically in the medium of $\beta'' \leq 0.198$, the acoustic slow mode generated directly from this pressure enhancement can be approximated well by one-dimensional hydrodynamics. That is, the difference of the velocity amplitude of the slow wave between two cases of one-dimensional simulation and our two-dimensional simulations was within 10 %. The spatial growth of the slow wave during its propagation upward through the low β'' chromospheric media also agrees well with that obtained from the one-dimensional hydrodynamic simulations. A magnetic fast mode does not play an important role for the overall dynamics and the energy transfer.

(3) In the case that an initial pressure (temperature) enhancement is located in high β' media, hydrodynamic buoyancy causes a vortex motion of gas, i.e. a modified internal gravity wave is generated. The vortex motion or the bubble dynamics is strongly influenced by magnetic field if the magnetic pressure is larger than the dynamic pressure.

In many previous one-dimensional hydrodynamic simulations of solar jet phenomena (Suematsu et al., 1982; Shibata et al., 1982; Shibata and Suematsu, 1982a; Shibata, 1982), it was assumed that slow shocks, which lead to spicule-like jet phenomena, are generated by a sudden pressure enhancement (or an impulsive heating of gas) associated with an appearance of a bright point in a strong magnetic flux tube. The above result (2) provides a basis for this assumption. However, the above result (1) might provide an alternative or additional mechanism of the generation of slow shocks that lead to spicules, because acoustic waves are generally believed to exist everywhere in the non-magnetic solar atmosphere (e.g. Kuperus et al., 1981) and thus slow shocks would be efficiently produced from these acoustic waves at the level of $\beta^{*''} \approx 1$ if the field line crosses that level.

The generation of slow waves (or shocks) at $\beta^{*''} \approx 1$ level might also contribute to the heating of the chromosphere and the corona. The possibility of coronal and/or chromospheric heating by acoustic slow shocks has been already studied by many authors (e.g. Osterbrock, 1961; Pikelner and Livshitz, 1964; Uchida and Kaburaki, 1974; Ulmschneider and Bohn, 1981; Ulmschneider and Stein, 1982; Hollweg et al., 1982; Hollweg, 1982; Shibata and Suematsu, 1982b). However, our result that acoustic fast waves generated in high $\beta^{*'}$ media mainly become acoustic slow waves when propagating upward into low $\beta^{*''}$ media in vertical field regions seems to have a renewed interest on the possibility of atmospheric heating by slow shocks, because, as mentioned before, acoustic waves are generally believed to exist everywhere in high $\beta^{*''}$ media and to heat the low chromosphere (Ulmschneider, 1970, 1971, 1974, 1979; Kuperus et al., 1981).

Many observations of atmospheric oscillations in the upper chromosphere and transition regions (Athay and White, 1978, 1979a, b, 1980; Schmieder and Mein, 1980; Mein and Schmieder, 1981; Bruner, 1981; Bonnet, 1981) show that the energy flux of acoustic waves is insufficient to heat the upper chromosphere and corona. As pointed out by Ulmschneider (1979), however, the spatial resolution of these observations is too crude to derive the real energy flux. In fact, slow shocks can be confined into very small cross-sectional area as shown in this paper. We should note here the following present circumstances : even the hypothesis that spicules are produced by slow shocks (Suematsu et al., 1982; Shibata and Suematsu, 1982a; Shibata, 1982) is not yet confirmed by observations. In this regard, Deubner (1974) reported an interesting observational fact " a disturbance, starting as a 'granular ring' in the photosphere, propagates upward to the top of the chromosphere, where a 'spicule' is formed ". More detailed observations will be necessary.

This paper has studied MHD wave generation and propagation in the solar chromosphere in very restricted parameter ranges. Therefore, we must investigate the cases of more general situations and also more special ones, although we believe that basic results found in this paper would not be essentially changed by simple generalizations.

The author wishes to express his hearty thanks to Professor S. Kato for his kind and critical reading of the manuscript. He also thanks Professors Y. Uchida and T. Hirayama, and Dr. T. Sakurai for valuable discussions. Thanks are also due to Drs. M. T. Nishida and Y. Watanabe for providing him with their graphics program. This work was carried out under a collaborating research program at the Institute of Plasma Physics, Nagoya University.

References

Ando, H. and Osaki, Y. 1975, Publ. Astron. Soc. Japan, 27, 581.

Athay, R. G. and White, O. R. 1978, Astrophys. J., 226, 1135.

Athay, R. G. and White, O. R. 1979a, Astrophys. J. Suppl., 39, 333.

Athay, R. G. and White, O. R. 1979b, Astrophys. J., 229, 1149.

Athay, R. G. and White, O. R. 1980, Astrophys. J., 240, 306.

Bonnet, R. M. 1981, Space Sci. Rev., 29, 131.

Bruner, E. C. 1981, Astrophys. J., 247, 317.

Chu, C. K. 1978, Advances in Applied Mechanics, 18, 285.

Deubner, F. L. 1974, in Chromospheric Fine Structure, IAU Symp. No. 56, ed. R. G. Athay (D. Reidel Publ. Co., Dordrecht), p. 263.

Deubner, F. L. 1977, in The Energy Balance and Hydrodynamics of the Solar Chromosphere and Corona, IAU Colloq. No. 36, ed. R. M. Bonnet, and Ph. Delache (Clermont-Ferrand: de Bussac), p. 45.

Dryer, M., Wu, S. T., Steinolfson, R. S., and Wilson, R. M. 1979, Astrophys. J., 227, 1059.

Gingerich, O., Noyes, R. W., Kalkofen, W., and Cuny, Y. 1971, Solar Phys., 18, 347.

Hollweg, J. V. 1982, Astrophys. J., 257, 345.

Hollweg, J. V., Jackson, S., and Galloway, D. 1982, Solar Phys., 75, 35.

Kaburaki, O. and Uchida, Y. 1971, Publ. Astron. Soc. Japan, 23, 405.

Kato, S. 1966, Astrophys. J., 144, 326.

Kuperus, M., Ionson, J. A., and Spicer, D. S. 1981, Ann. Rev. Astron. Astrophys., 19, 7.

Lamb, H. 1932, Hydrodynamics (Dover, New York), p. 541.

Mein, N. and Schmieder, B. 1981, Astron. Astrophys., 97, 310.

Nakagawa, Y. 1980, Astrophys. J., 240, 275.

Nakagawa, Y. 1981a, Astrophys. J., 247, 707.

Nakagawa, Y. 1981b, Astrophys. J., 247, 719.

Nakagawa, Y., Wu, S. T., and Han, S. M. 1978, Astrophys. J., 219, 314.

Nakagawa, Y., Wu, S. T., and Han, S. M. 1981, Astrophys. J., 244, 331.

Osterbrock, D. E. 1961, Astrophys. J., 134, 347.

Pikelner, S. B. and Livshitz, M. A. 1965, Soviet Astron., 8, 808.

Roache, P. J. 1972, Computational Fluid Dynamics (Hermosa Publishers, Albuquerque, New Mexico).

Rubin, E. L. and Burstein, S. Z. 1967, J. Comp. Phys., 2, 178.

Sato, T. and Hayashi, T. 1979, Phys. Fluids, 22, 1189.

Schmieder, B. and Mein, N. 1980, Astron. Astrophys., 84, 99.

Shibata, K. 1981, in Proceedings of The Japan-France Seminar on Solar Physics, ed. F. Moriyama and J. C. Henoux (Tokyo Astronomical Observatory, Mitaka), p. 50.

Shibata, K. 1982, Solar Phys., 81, 9.

Shibata, K. and Suematsu, Y. 1982a, Solar Phys., 78, 333.

Shibata, K. and Suematsu, Y. 1982b, submitted to Solar Phys.

Shibata, K., Nishikawa, T., Kitai, R., and Suematsu, Y. 1982, Solar Phys., 77, 121.

Stein, R. F. 1971, Astrophys. J. Suppl., 22, 419.

Stein, R. F. 1981, Astrophys. J., 246, 966.

Stein, R. F. and Leibacher, J. 1974, Ann. Rev. Astron. Astrophys., 12, 407.

Stein, R. F. and Schwartz, R. A. 1972, Astrophys. J., 177, 807.

Steinolfson, R. S., Wu, S. T., Dryer, M., and Tandberg-Hanssen, E. 1978, Astrophys. J., 225, 259.

Suematsu, Y. 1982, private communication.

Suematsu, Y., Shibata, K., Nishikawa, T., and Kitai, R. 1982, Solar Phys., 75, 99.

Uchida, Y. 1968, Solar Phys., 4, 30.

Uchida, Y. and Kaburaki, O. 1974, Solar Phys., 35, 451.

Ulmschneider, P. 1970, Solar Phys., 12, 403.

Ulmschneider, P. 1971, Astron. Astrophys., 14, 275.

Ulmschneider, P. 1974, Solar Phys., 39, 327.

Ulmschneider, P. 1979, Space Sci. Rev., 24, 71.

Ulmschneider, P. and Bohn, H. U. 1981, Astron. Astrophys., 99, 173.

Ulmschneider, P. and Stein, R. F. 1982, Astron. Astrophys., 106, 9.

Wu, S. T., Dryer, M., Nakagawa, Y. and Han, S. M. 1978, Astrophys. J., 219, 324.

Figure Captions

Fig. 1 Height variations of plasma β^* ($= 8\pi p/B^2$) (solid curve) and Alfven velocity V_A ($= B/\sqrt{4\pi\rho^*}$) (broken curve with dot) in the photosphere and the chromosphere. The height is measured from the level of $\tau^*_{5000} = 1$. Numerals beside curves represent the initial field strength B_0.

Fig. 2 Two dimensional spatial contour maps of gas pressure ($\Delta p/p_0$) at various times, (a) 0.0 sec, (b) 16.49 sec, (c) 32.98 sec, (d) 49.46 sec for $B_0 = 90.7$ G, where $\Delta p = p - p_0$ and p_0 is the initial value of pressure. The ordinate corresponds to the height (y) axis and the abscissa to the horizontal (x) axis. The interval of level of contour curves is 0.02 in units of p_0. Solid curves show positive Δp and dashed curves represent negative Δp.

Fig.3 Two-dimensional spatial velocity fields at t = 16.49, 32.98, 49.46 sec for $B_0 = 90.7$ G. The arrow represents the velocity vector, and its magnitude is shown in the upper left part of (a). Only velocities greater than 0.1 km s^{-1} are shown. Other remarks are the same as in figure 2.

Fig. 4 Spatial contour maps of (a) magnetic field strengths $\Delta B/B_0$, (d) gas pressure $\Delta p/p_0$, and (b) velocity fieds, (c) spatial configuration of field lines, at t = 57.68 sec for $B_0 = 90.7$ G, where $\Delta B = B - B_0$, $B = (B_x^2 + B_y^2)^{1/2}$, and the subscript 0 represents the initial unperturbed value. Dashed curves in (a) and (d) represent negative values, and the intervals of level of contour curves are all 0.02 in units of their initial values. Dashed curves in (c) shows the initial field lines. Other remarks are the same as in figure 3. Note that the results near upper boundary ($y \gtrsim 1100$ km) are not reliable due to insufficient

boundary condition.

Fig. 5 Three dimensional plot of $\Delta p/p_0$ for (a) $B_0 = 0$ G and (b) $B_0 = 90.7$ G. Numerals denote the time (sec). The arrow in (a) t = 0.0 sec denotes the direction of height (y) coordinate. The illustrated area of each three dimensional plot is the same as that of the two-dimensional contour maps in figures 2 - 4. The scale of $\Delta p/p_0$ can be found from the figure of t = 0.0 sec because $(\Delta p/p_0)_{max} = 0.5$ and $(\Delta p/p_0)_{min} = 0.0$ at t = 0.0. Note the generation of acoustic slow mode at about t = 49.46 sec in (b).

Fig. 6 Velocity fields and contour maps of $\Delta T/T_0$ at t = 73.41, 94.28, 113.53, and 137.10 sec for $B_0 = 90.7$ G. Only lower half part of calculated domain is indicated. Other remarks are the same as in figure 4.

Fig. 7 Velocity fields and contour maps of $\Delta T/T_0$ at t = 71.44, 95.67, 117.86, and 139.56 sec for $B_0 = 0$. Other remarks are the same as in figure 6.

Fig. 8 Velocity fields and contour maps of $\Delta p/p_0$ at t = 5.12, 10.23, 15.32 and 20.36 sec for $B_0 = 907$ G. The regions near upper boundary ($600 \leq y \leq 750$ km) are omitted in these figures. Other remarks are the same as in figure 4.

Fig. 9 Time variations of various physical quantities (v_y: vertical velocity, B_y: vertical component of magnetic field strength, p: gas pressure, ρ': density, T: temperature) at explosion point (center of the initial pressure enhancement) for $B_0 = 90.7$ G (solid curves) and 907 G (dashed curves). The subscript 0 represents the initial value at the height outside the initial pressure enhancement region.

Fig. 10 Log-log plot of v_{amp}/c against ρ^{+1} in the case of Cartesian coordinate, where v_{amp} is the velocity amplitude at the slow wave front, and c and ρ^{+1} are the sound velocity and density, respectively, at the upperturbed chromosphere where the wave pases. Black circles (1HD), black squares (B_0 = 0 G), white squares (B_0 = 907 G), white circles (B_0 = 363 G), black triangles (B_0 = 181 G), white triangles (B_0 = 90.7 G).

Fig. 11 Log-log plot of v_{amp}/c aganst ρ^{+1} in the case of cylindrical coordinate with axial symmetry. Other remarks are the same as in figure 10.

Fig. 12 Time variations of horizontally integrated energy flux at various fixed heights. (a) B_0 = 0 G, (b) B_0 = 90.7 G, (c) B_0 = 907 G, in the case of Cartesian coordinate. Thick curves represent $F = \Delta p\, v_y$, and thin curves denote $F = -B_x B_{y0} v_x/4\pi$.

Table I Summary of Simulation Results

B_0 (Gauss)	β_0	β_*	$y_{\beta=1}$ (km)	vortex motion		t_c (sec)		v_{slow}/v_{1HD} at y = 600 km	
				xy	rz	xy	rz	xy	rz
0	∞	∞	∞	yes	yes	131	122	0.52	0.24
90.7	400	19.8	665	yes	yes	110	107	0.52	0.24
181.4	100	4.95	520	yes	yes	86	85	0.62	0.39
362.8	25	1.24	380	no	no	83	80	0.76	0.68
907	4	0.198	180	no	no	78	**	0.93	0.91
∞	0	0.0	---	------		77		1.00	

β_0 : $8\pi p/B^2$ at y = 0 km

β_* : $8\pi p/B^2$ at y = 345 km, where the center of explosion is located

$y_{\beta=1}$: height where $\beta^{\neq}(8\pi^{\neq}p/B^2) = 1$

t_c : time when the vertical velocity at explosion point changes its sign

** : the simulation in this case was terminated by numerical instability before v_y becomes negative

Fig. 1

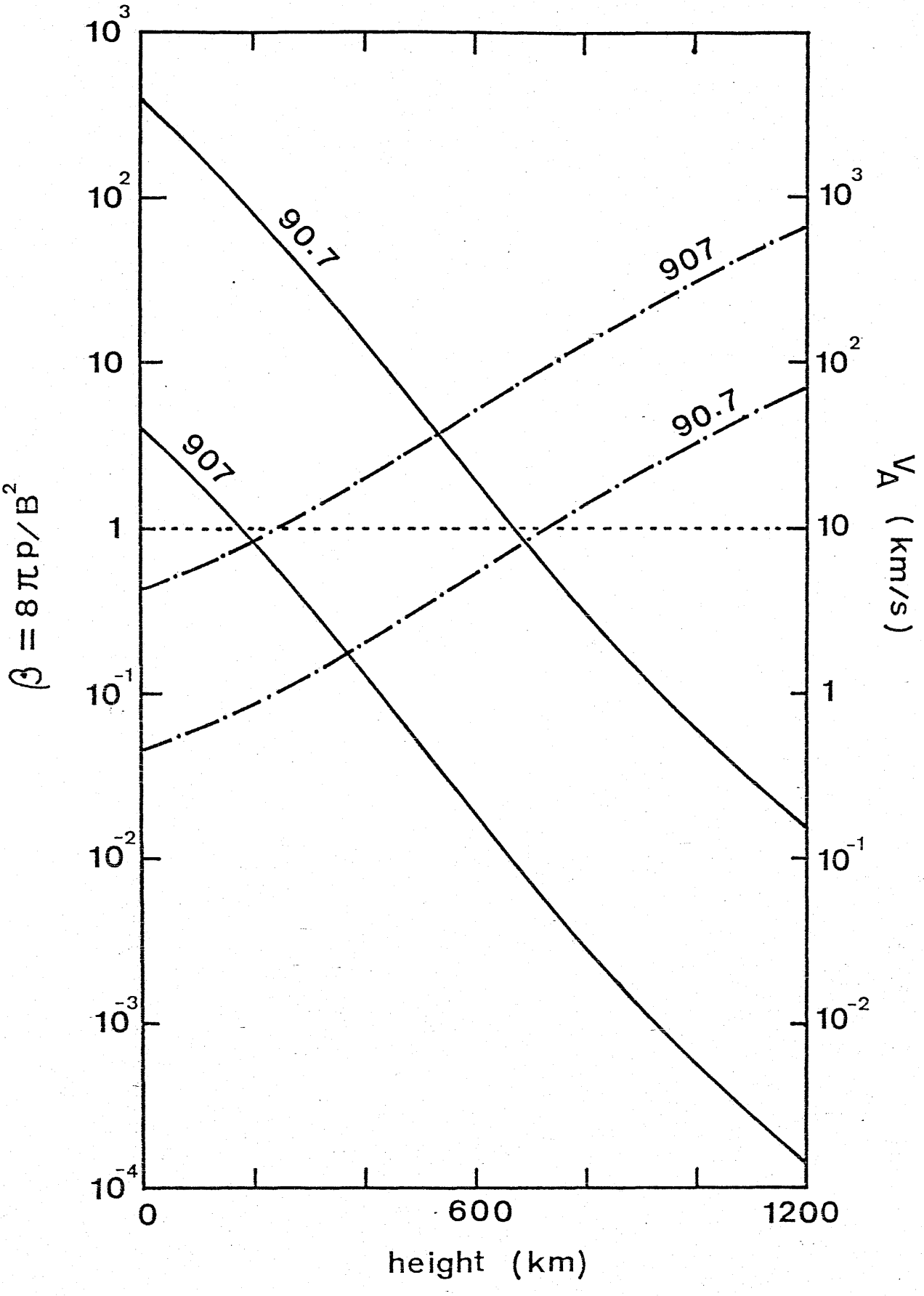
10^3
10^2
10
1
10^{-1}
10^{-2}
10^{-3}
10^{-4}
$\beta = 8\pi p/B^2$
90.7
907
907
90.7
10^3
10^2
10
1
10^{-1}
10^{-2}
V_A (km/s)
0
600
1200
height (km)

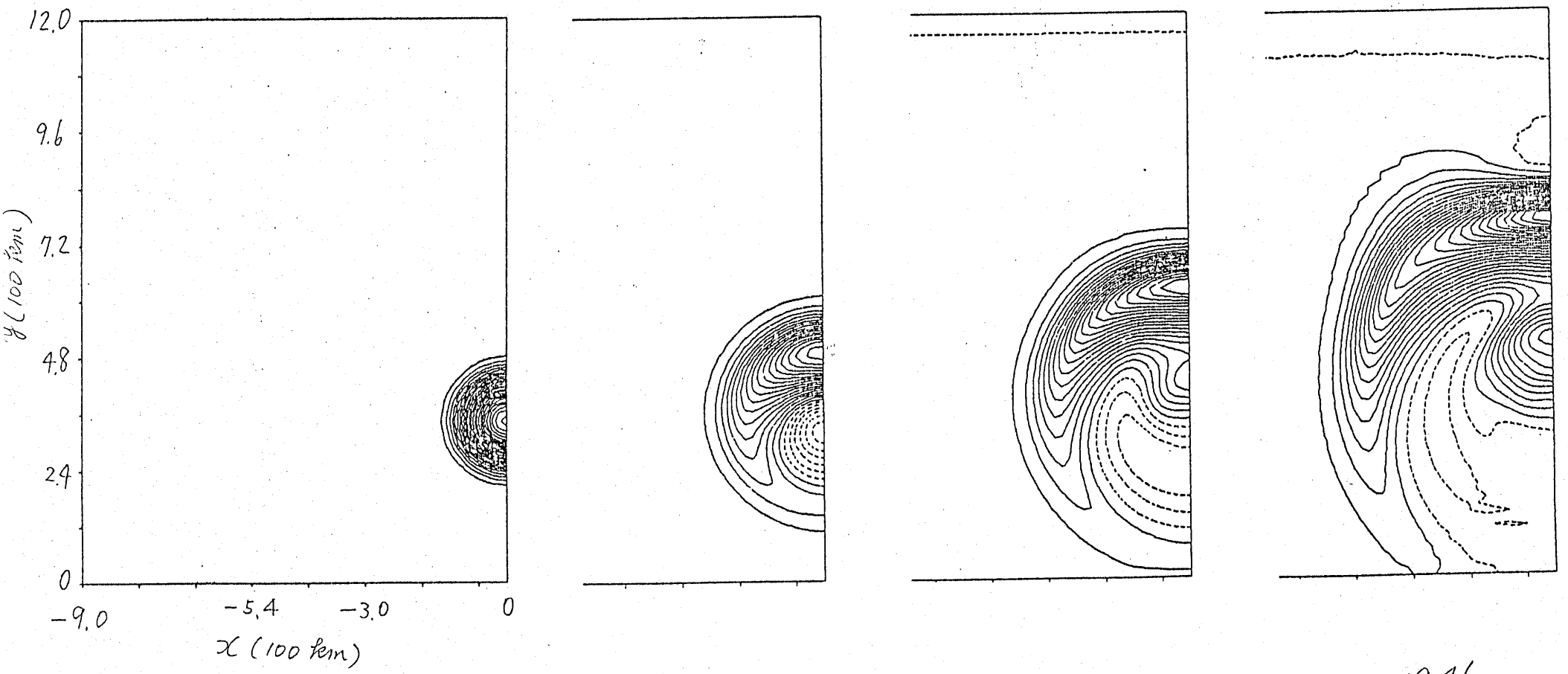

(a) 0.0 sec

(b) 16.49

(c) 32.98

(d) 49.46

Fig. 2

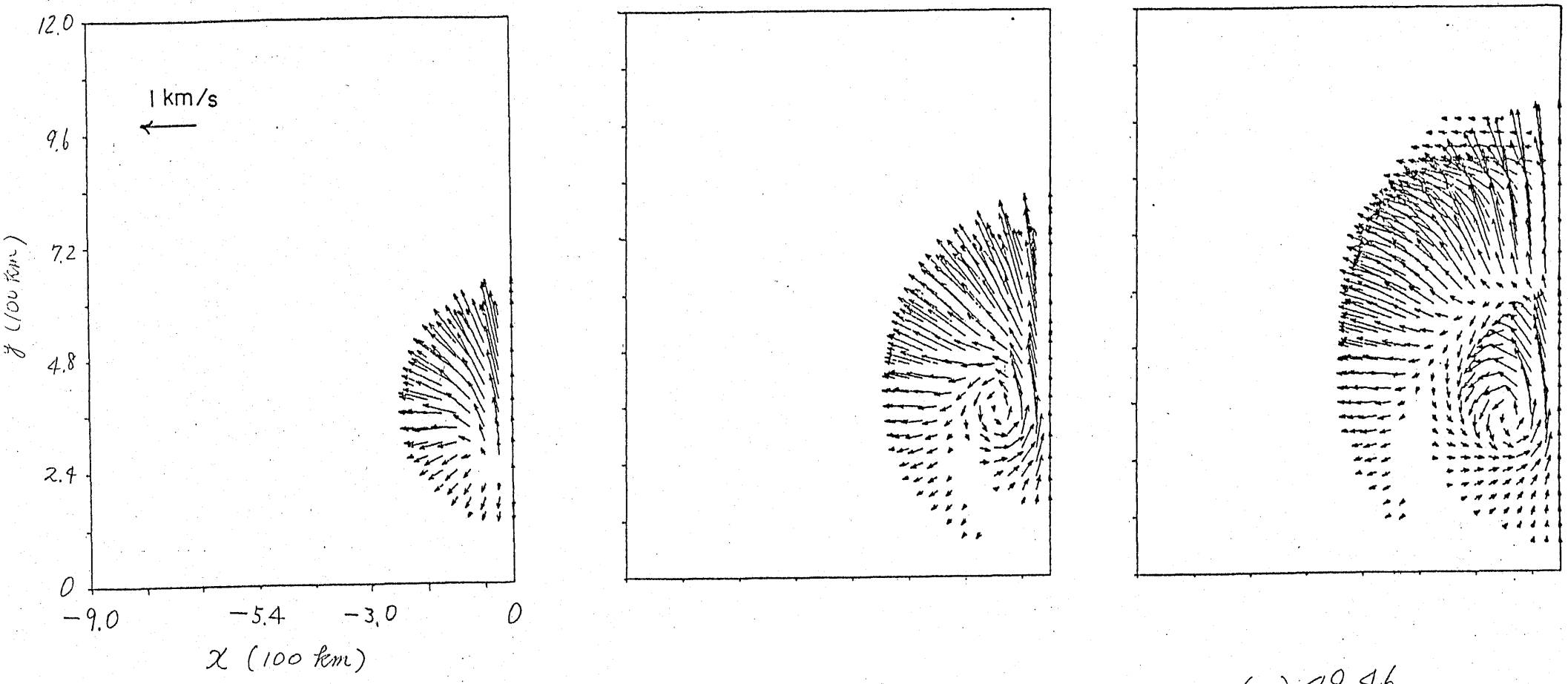

(a) 16.49 sec

(b) 32.98

(c) 49.46

Fig. 3

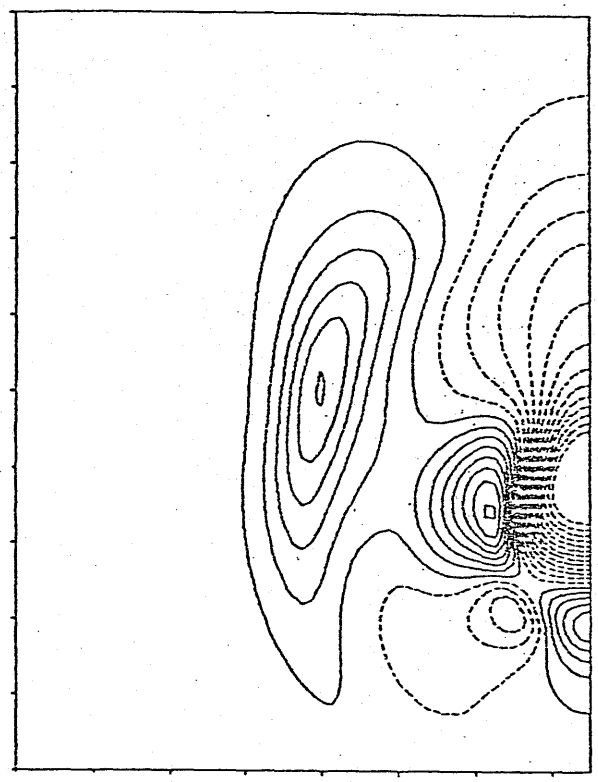

(a) MAGNETIC FIELD STRENGTH

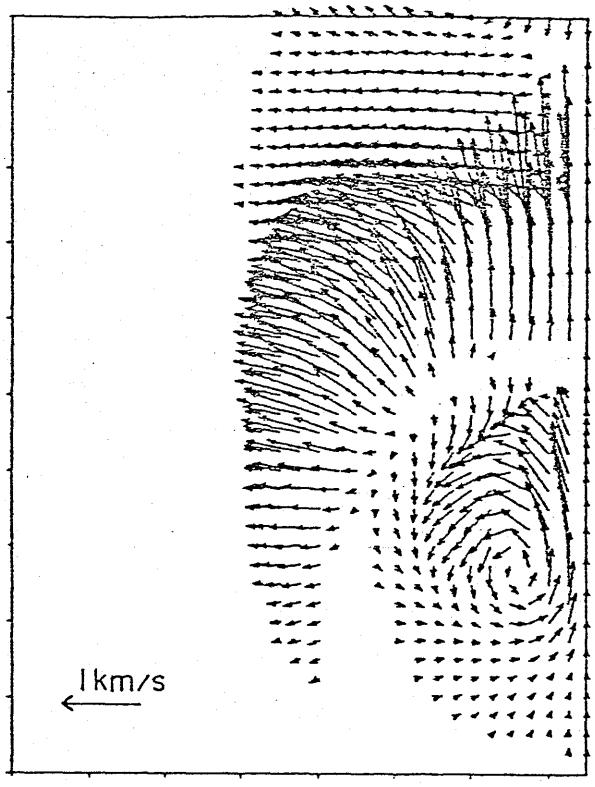

(b) VELOCITY VECTOR

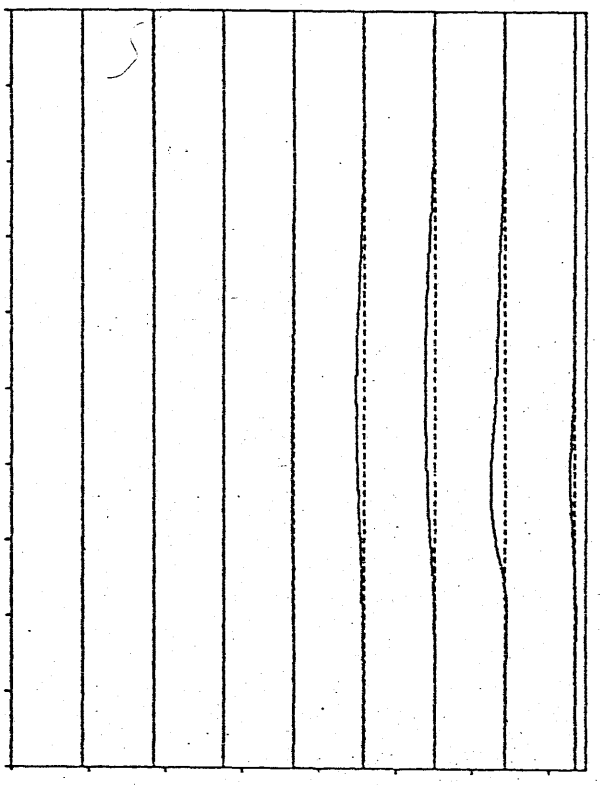

(c) FIELD LINE

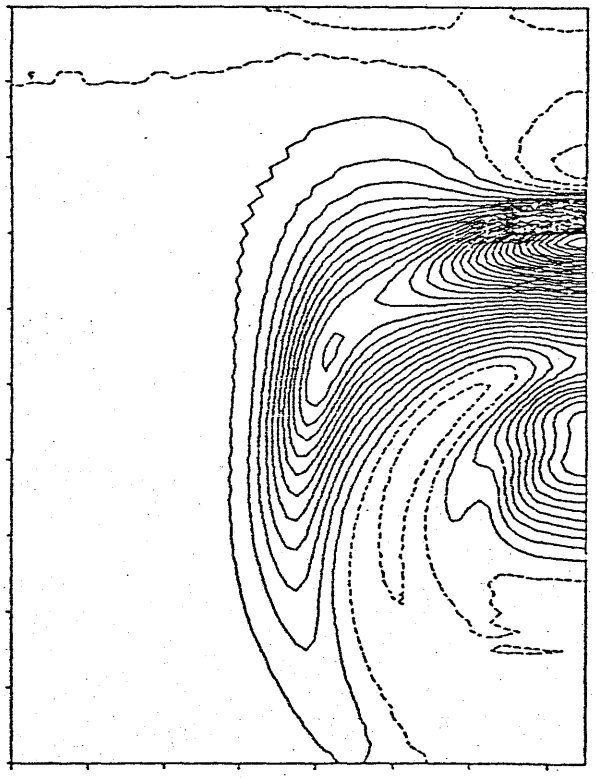

(d) GAS PRESSURE

Fig. 4

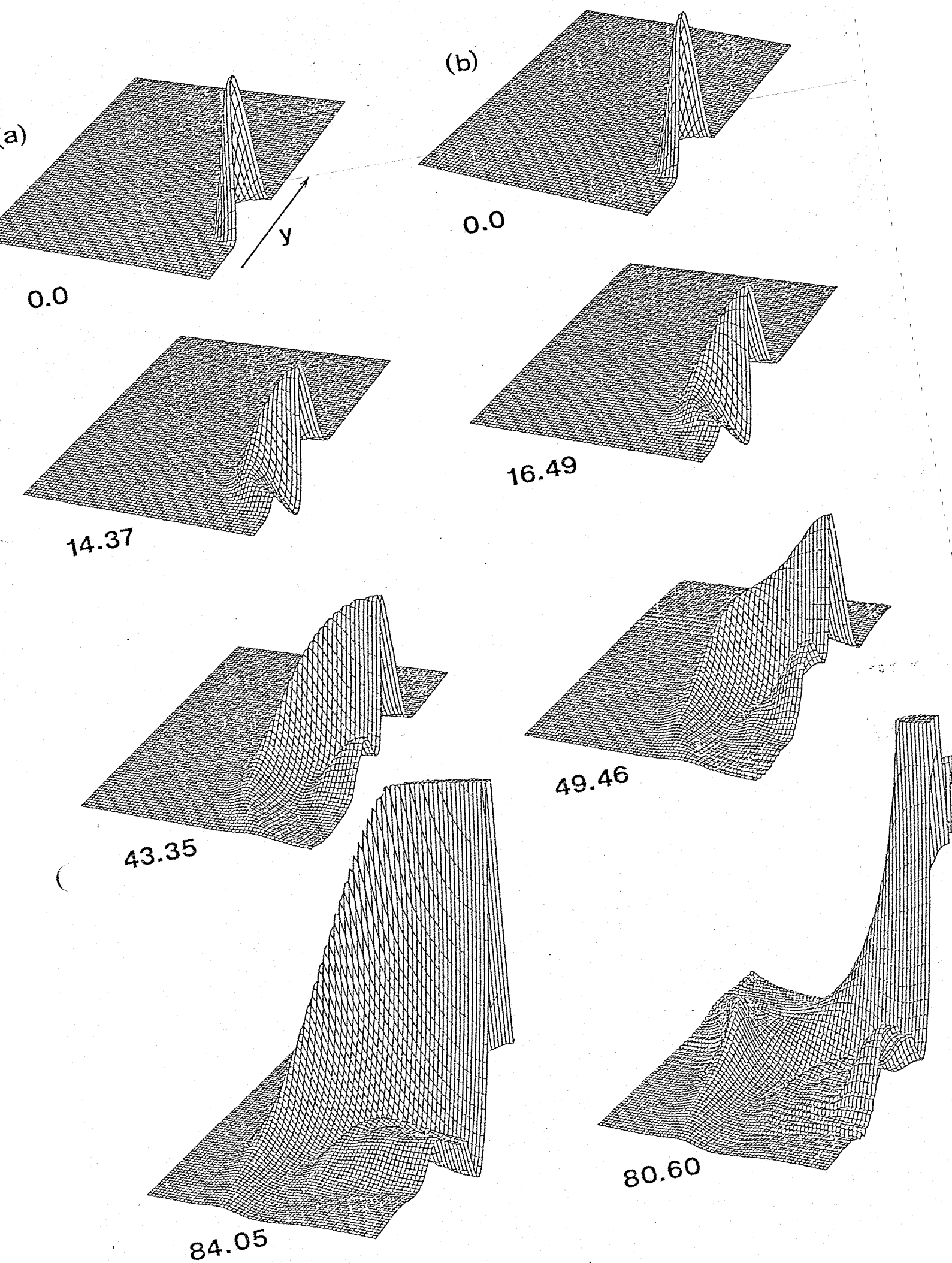

Fig. 5

Fig. 6

VELOCITY VECTOR

TEMPERATURE

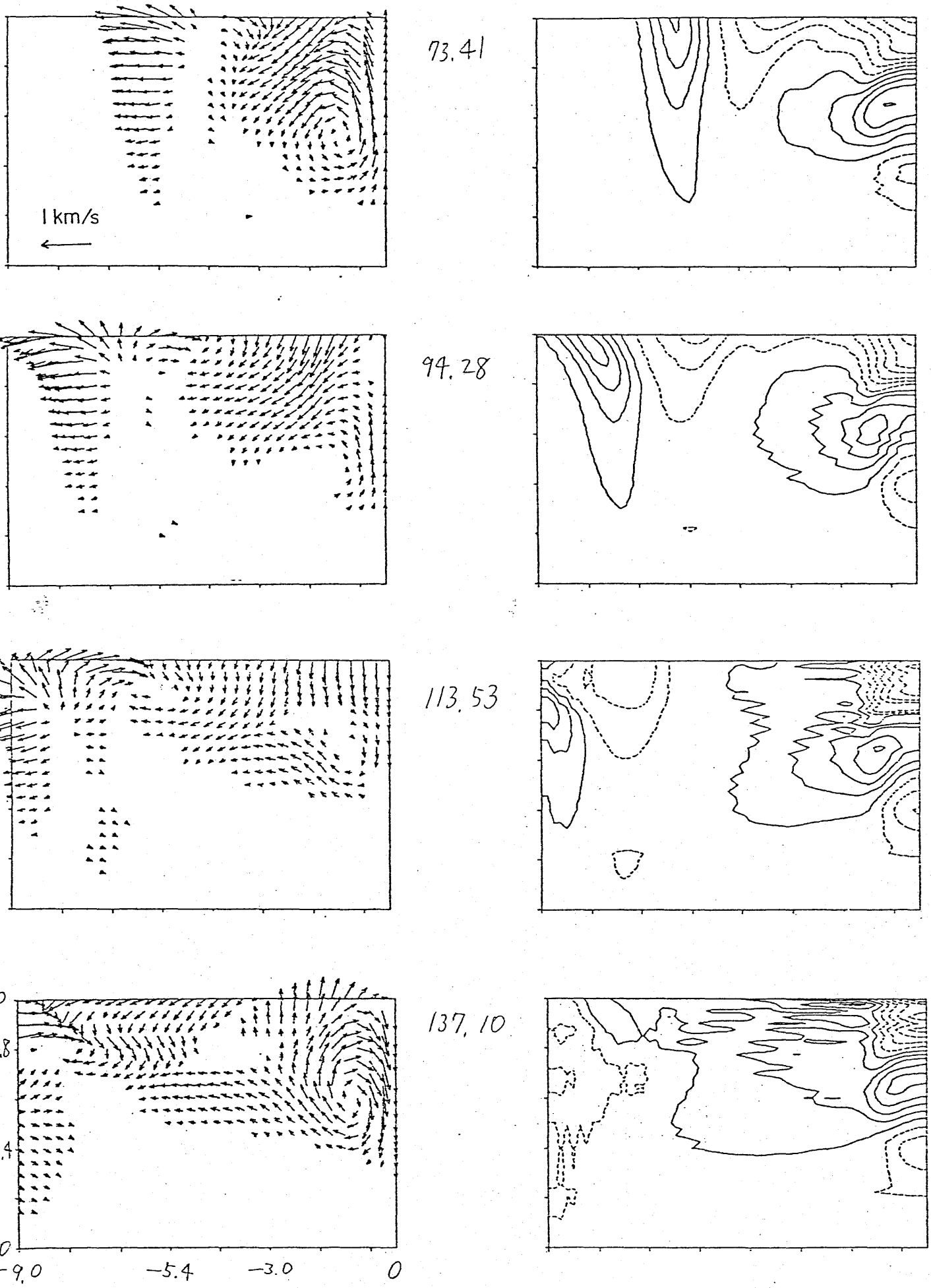

Fig. 6

Fig. 7

VELOCITY VECTOR

TEMPERATURE

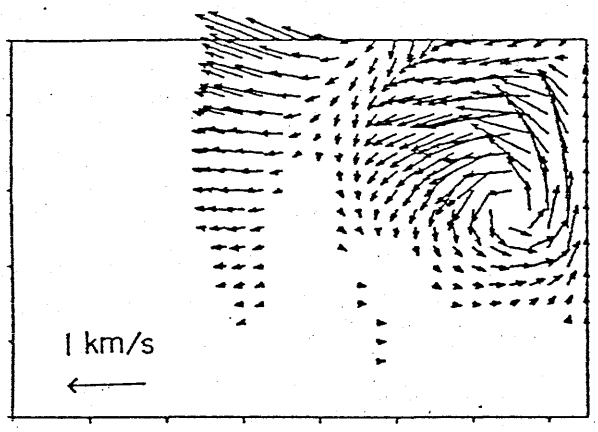

71, 44

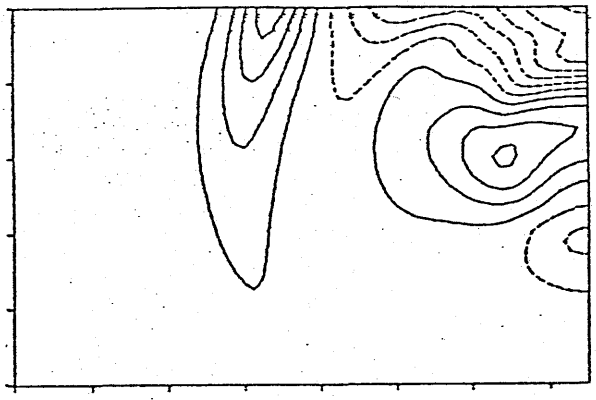

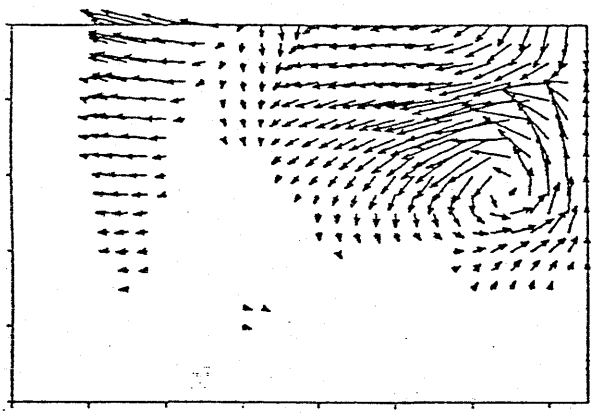

95, 67

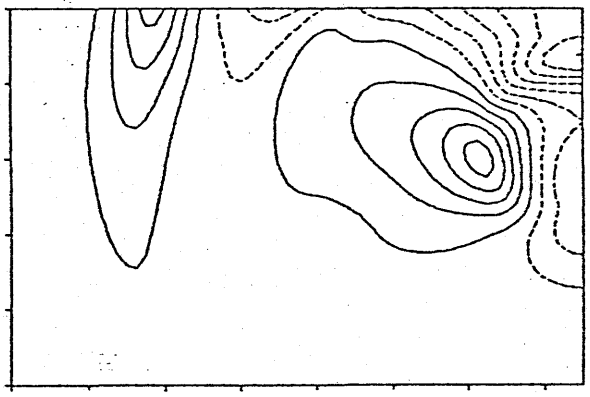

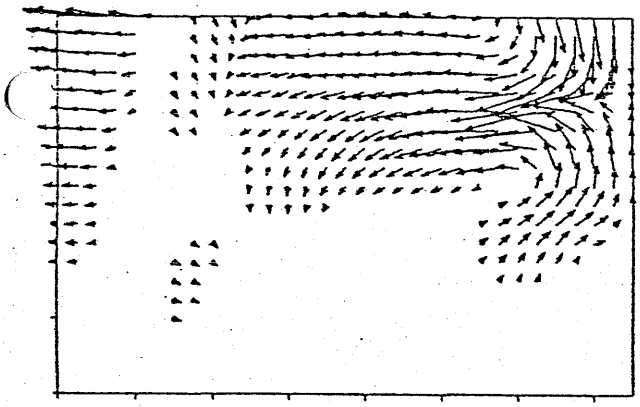

117. 86

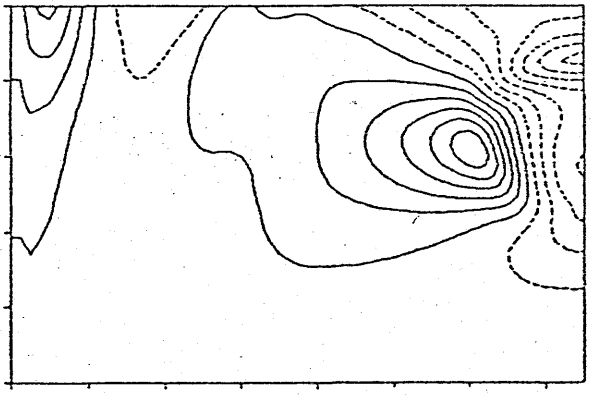

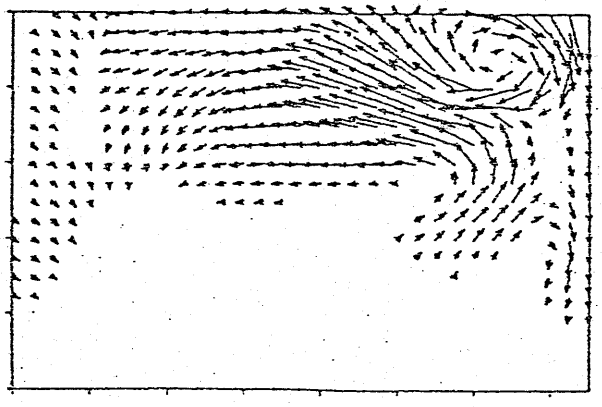

139. 56

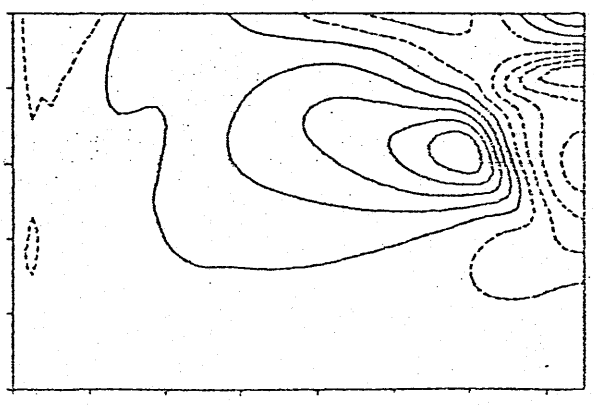

Fig. 8

VELOCITY VECTOR

GAS PRESSURE

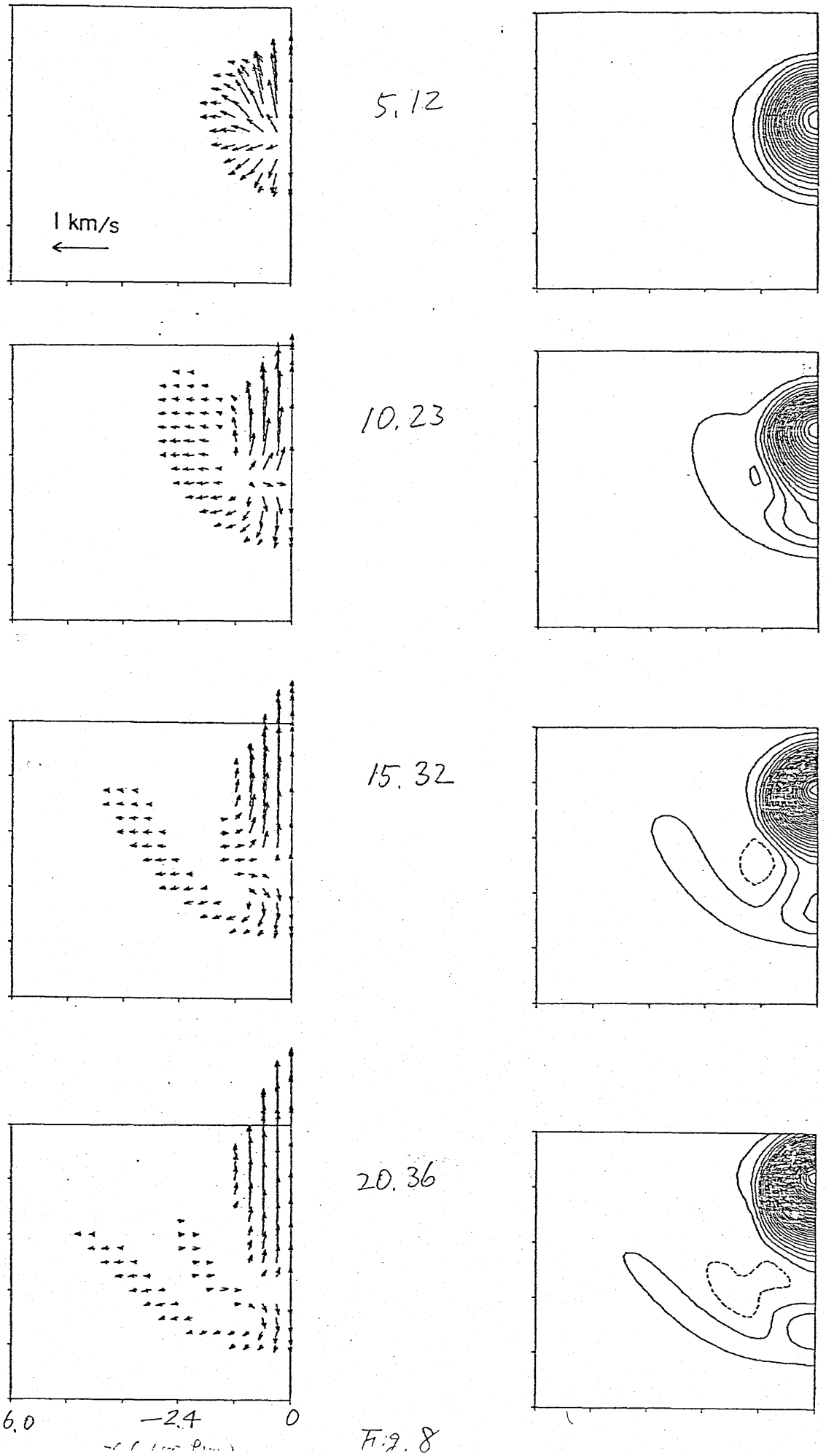

Fig. 8

Fig. 9

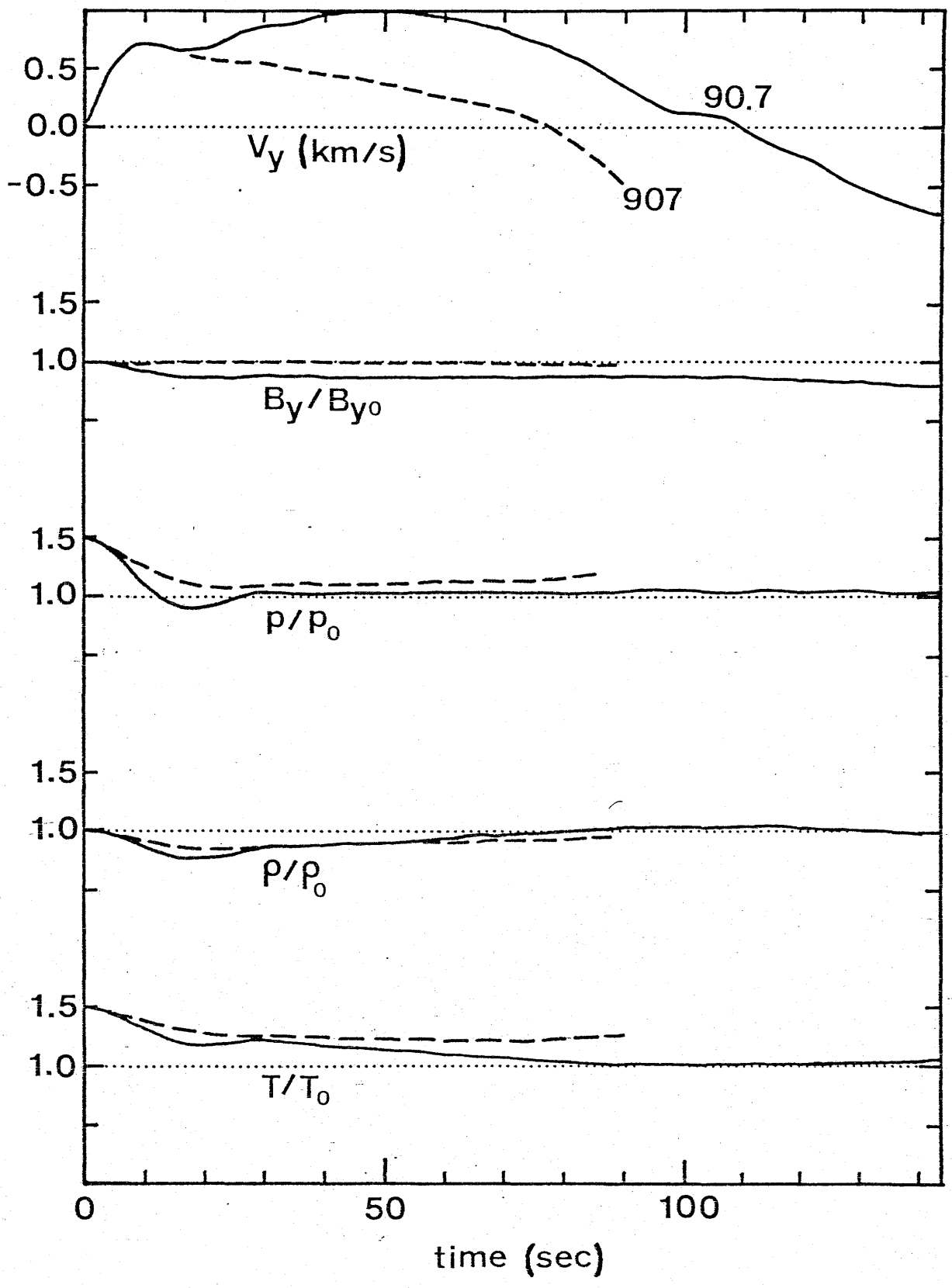
0.5
0.0
-0.5
V_y (km/s)
90.7
907
1.5
1.0
B_y/B_{yo}
1.5
1.0
p/p_o
1.5
1.0
ρ/ρ_o
1.5
1.0
T/T_o
0
50
100
time (sec)

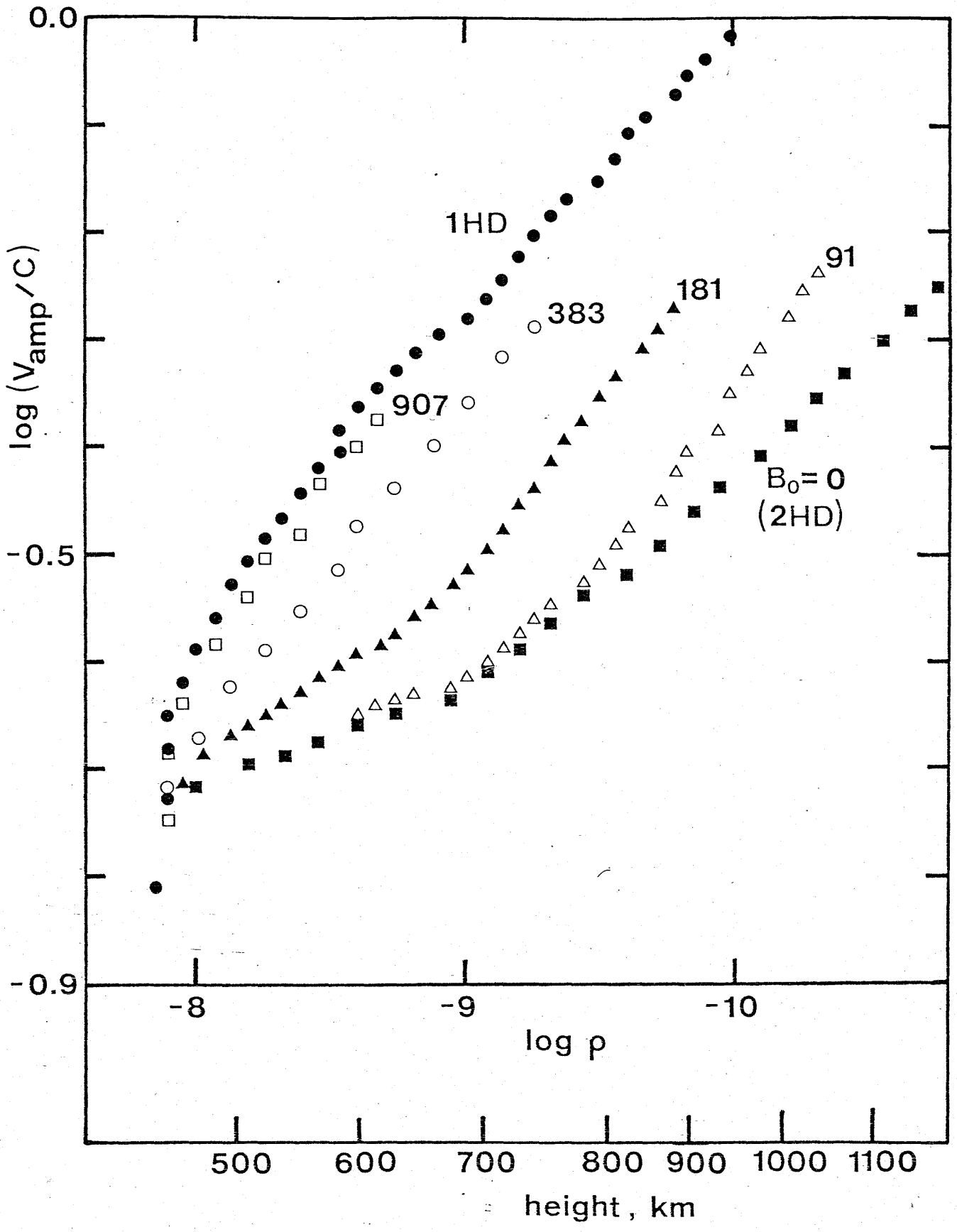
0.0
-0.5
-0.9
log (V_{amp}/C)
1HD
383
907
181
91
B_0= 0
(2HD)
-8
-9
-10
log ρ
500
600
700
800
900
1000
1100
height, km

Fig. 10

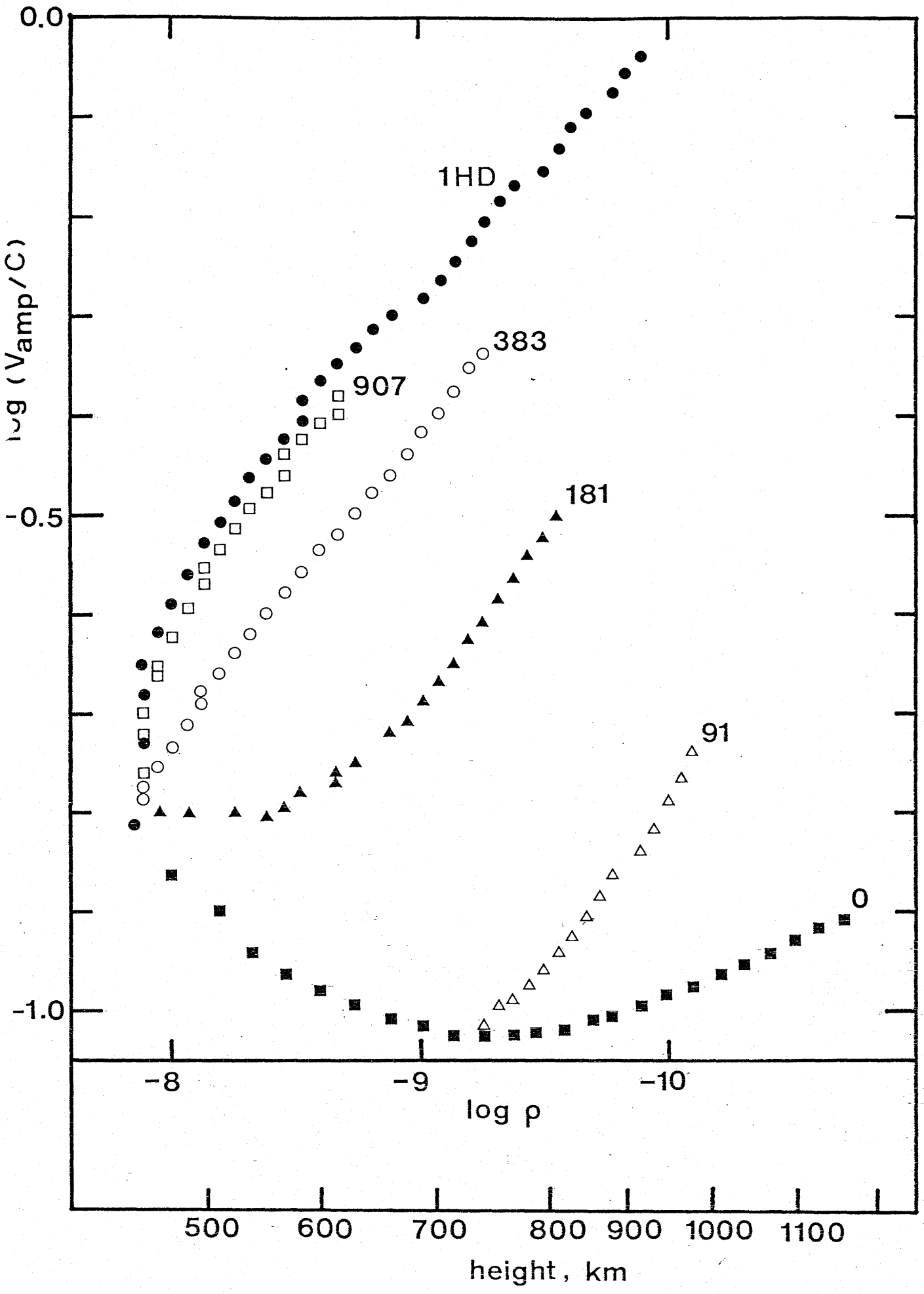
0.0
-0.5
-1.0
log (Vamp/C)
1HD
383
907
181
91
0
-8
-9
-10
log ρ
500
600
700
800
900
1000
1100
height, km

Fig. 11

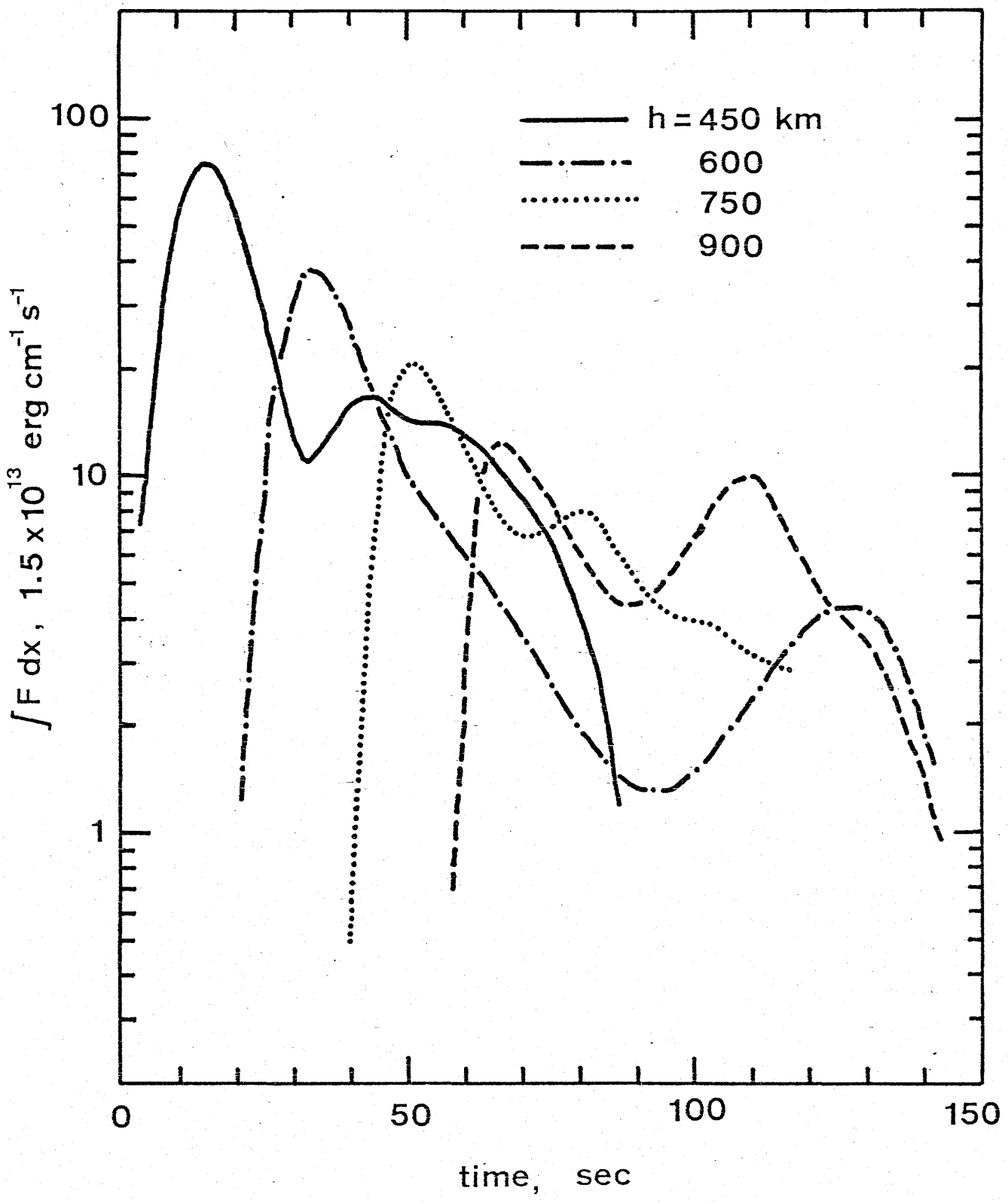
h = 450 km
600
750
900
100
10
1
0
50
100
150
time, sec
∫F dx, 1.5 x 10^13 erg cm^-1 s^-1

Fig. 12 (a)

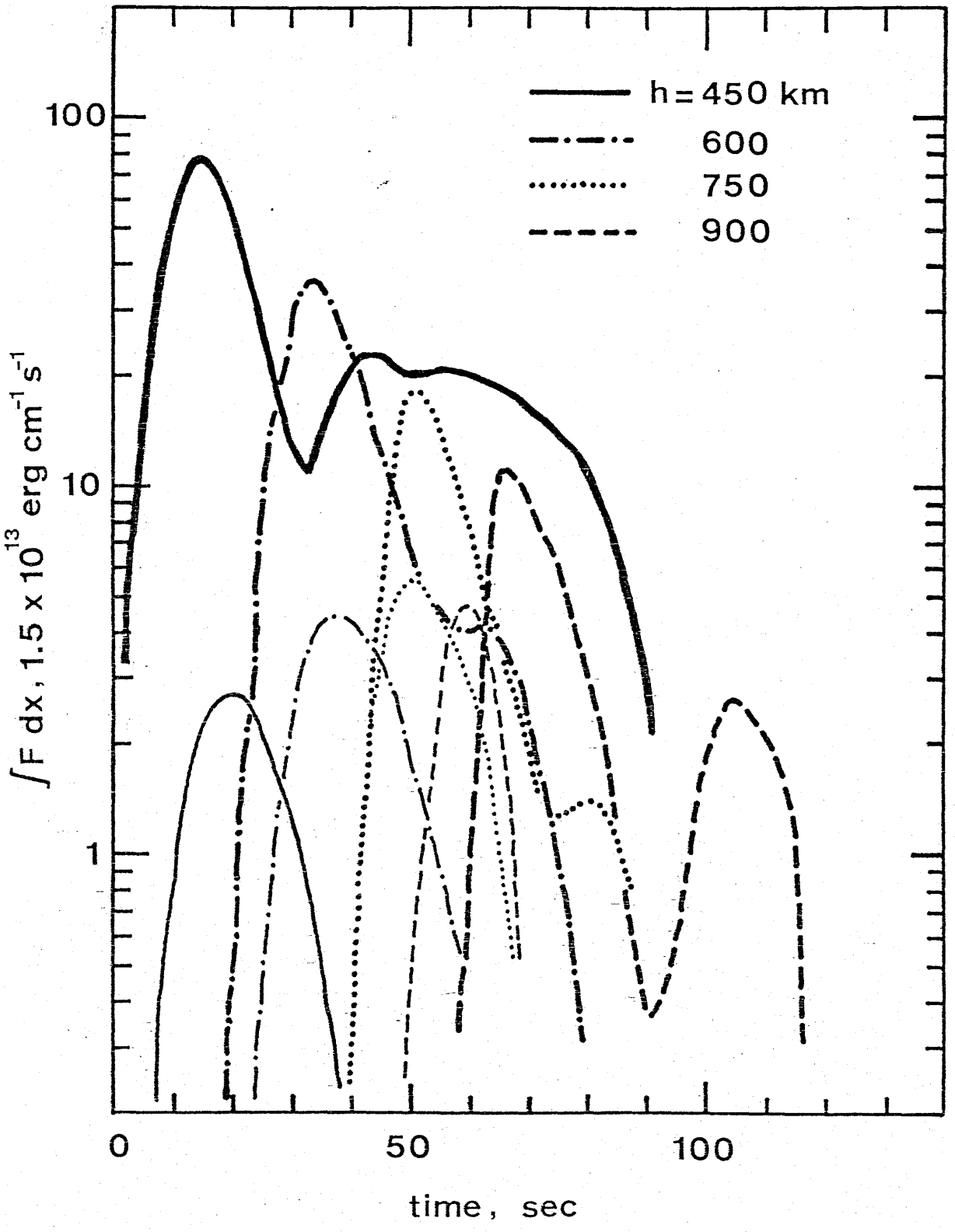
h = 450 km
600
750
900
100
10
1
0
50
100
time, sec
∫F dx, 1.5 x 10^13 erg cm^-1 s^-1

Fig. 12 (b)

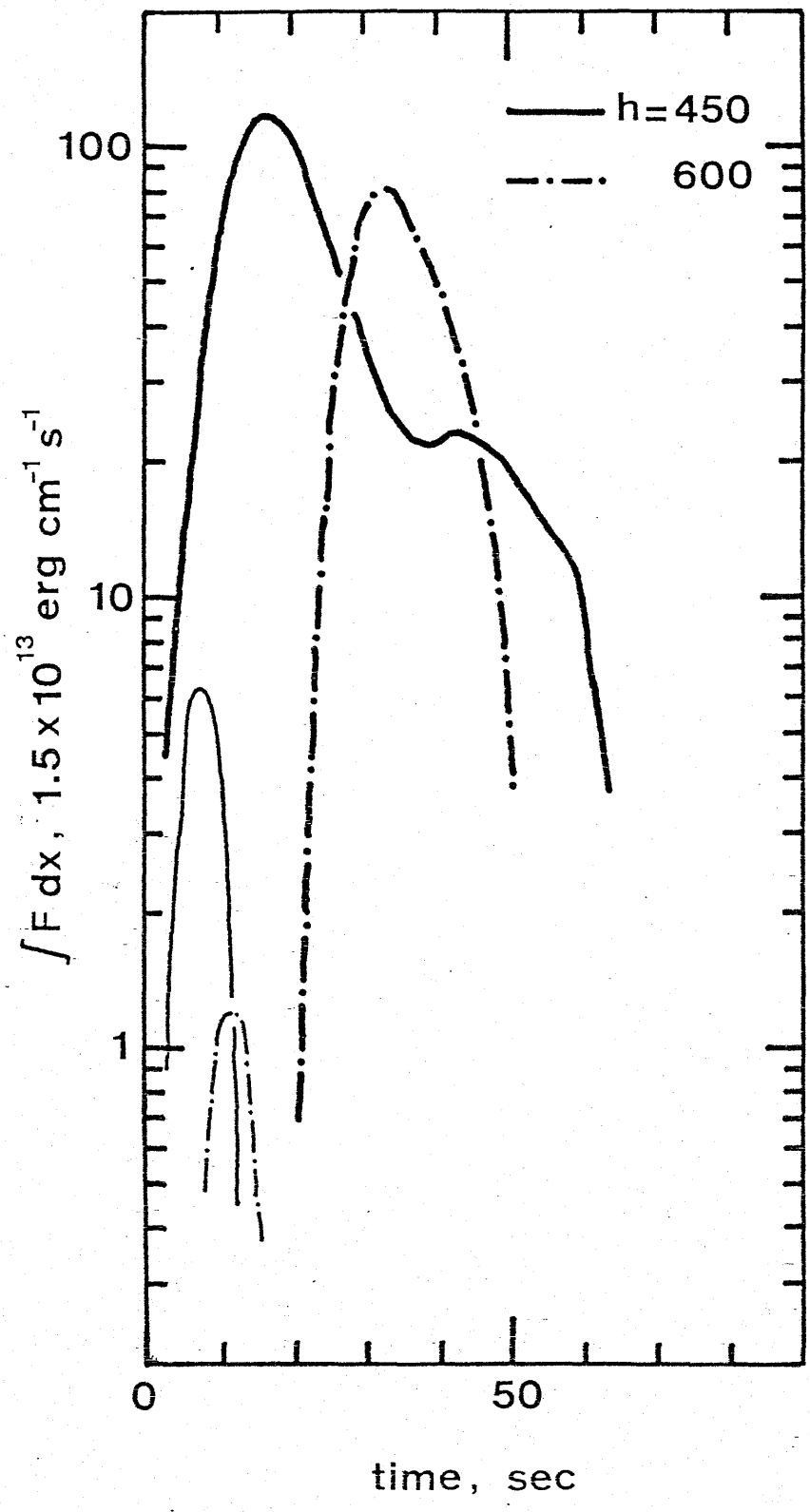

Fig. 12 (c)